Russian Chemical Reviews **78** (3) 249 – 282 (2009) © 2009 Russian Academy of Sciences and Turpion Ltd

DOI 10.1070/RC2009v078n03ABEH003901

Multifunctional nanomaterials

I P Suzdalev

Contents

I.	Introduction	249
II.	Multiferroics	249
III.	Spintronics	254
IV.	Piezoelectrics	259
V.	Magnetostrictors	261
VI.	Thermoelectric materials	270
VII.	Chemoelectrics	273
VIII.	Metamaterials	275

Abstract. Nanomaterials for which one can follow the mutual influence of electric, magnetic, thermal, mechanical, chemical and optical properties, namely, multiferroics, spintronics, piezoelectrics, magnetostrictors, thermo- and chemoelectrics and metamaterials are considered. Examples of nanodevices using multifunctional nanomaterials are given. The bibliography includes 134 references.

I. Introduction

Specific properties of nanomaterials are to a great extent due to the effects related to a decrease in the size of nanoparticles and structural fragments, the effect of surface and the comparability of the size of structural fragments with the size of charge carriers (electrons, phonons, excitons, magnons, *etc*.).[1,2] Multifunctional nanomaterials are not only practically valuable, but also of great interest for research and solution of many fundamental problems in physics and chemistry of the solid state. Such materials, as multiferroics or spintronics, are used as electric and magnetic switches whose electric and magnetic properties can be controlled by varying external magnetic and electric fields. Piezotronics relate the action of electric fields to mechanical motion and, *vice versa*, can generate e.m.f. when mechanically activated.

The volume of novel magnetostrictive materials (magnetostrictors) changes by tens of per cent under the action of external magnetic fields. Therefore, magnetostrictors can, similarly to piezoelectrics, serve as energy transducers. At the same time, magnetostriction of a nanomaterial causes such effects, as, *e.g*., first-order magnetic phase transitions, which are accompanied by jumpwise changes in the magnetisation of the material depending on the temperature or the size of the nanoclusters that form the nanostructure.

There is increasing progress in studies of thermoelectrics, which become practically valuable as e.m.f. sources on heating or cooling particular pieces of nanomaterials. The use of nanostructured electrodes offers prospects for carrying out electrochemical reactions in modern lithium cells; such nanomaterials can be called 'chemoelectrics'. The year 2000 was marked by the design of a novel class of materials, *viz*., metamaterials, which are made of components that intrinsically use magnetic and electric resonances; these materials, capable of transmitting or reflecting electromagnetic radiation, can have negative dielectric and magnetic susceptibilities and the refractive index.

In this review we will consider the structures, properties and fields of application of the following multifunctional nanomaterials: multiferroics, spintronics, piezoelectrics (piezotronics), magnetostrictors, thermoelectrics (two-dimensional thermoelectrics and multilayers will be considered), chemoelectrics (use of cluster reactions in charging – discharging of electric cells) and metamaterials. Among the variety of nanomaterials, those mentioned were chosen not only because of their multifunctional character, but also because they provide good examples of interplay between the electric and magnetic properties.

II. Multiferroics

Piezoelectrics or magnetostrictors are characterised by the dependence of the electric polarisation or magnetisation on the volume. The former group includes ferroelectrics while the latter comprises ferromagnetics, antiferromagnetics and other magnetics. Transition to the disordered charge or spin state (so-called para-state) represents a phase transition accompanied by the change in the unit cell volume at the Curie or Néel temperature (T_C and T_N, respectively). Ferro-

I P Suzdalev N N Semenov Institute of Chemical Physics, Russian Academy of Sciences, ul. Kosygina 4, 119991 Moscow, Russian Federation. Fax (7-495) 938 21 56, tel. (7-495) 939 71 01, e-mail: suzdalev@chph.ras.ru

Received 16 October 2008
Uspekhi Khimii **78** (3) 266 – 301 (2009); translated by A M Raevskiy

electrics and magnetics with different properties can co-exist in the same material, a multiferroic or a magnetoelectric, respectively. The possibility of co-existence and interplay between the orientations of the electron and spin systems in these materials has been documented.[3,4]

Multiferroics can exist in two and more states that can be switched on and off in magnetic or electric fields, *e.g.*, in polarised, magnetic, mechanically strained state, *etc*. In these cases, the polarisation and magnetisation change as a result of the interaction between the spin and magnetic systems. This interaction can be accompanied by linear magnetoelectric effects,[5,6] changes in polarisation,[7,8] magnetodielectric effect[9,10] and by dielectric anomalies on magnetic phase transitions.[11,12]

Magnetoelectric effects were observed in perovskite-type multiferroics $BiFO_3$ (Ref. 13) and $BMnO_3$,[14] in borates,[15] in compounds $BaMF_4$ (M is a divalent transition metal),[16] in hexagonal oxides $LnMnO_3$ (Refs 10 and 17) and in rare-earth element molybdates.[18]

The electronic and spin systems can interact in a multiferroic single crystal or in ferroelectric and magnetic thin epitaxial films coated on corresponding substrates. In the case of heterosystems, there is an additional possibility of controlling this interaction by varying the film thickness (from 1 to 10 nm).

Monomultiferroics are crystalline substances in which the interaction between the electronic (lattice) and spin subsystems can induce spontaneous magnetisation and electric polarisation. In most cases, these effects occur at low temperatures, which makes their practical application difficult. However, such systems are of great interest for research on the nature and specific features of these effects. Now we will consider $TbMn_2O_5$ as an example of monomultiferroic.[19] This compound has a complex crystal structure of orthorhombic symmetry *Pbam*. Mn^{4+} ions are surrounded by hydrogen atoms (octahedral environment) while Mn^{3+} ions are located at the centres of the base (square) of a pyramid. In this compound in consequence of exchange interactions of Tb^{3+}, Mn^{3+} and Mn^{4+} spins and polarisation crystal lattice induce a number of phase transitions. At 2 K, a large magnetic anisotropy along the light axis *a* was discovered; the saturation magnetisation was 8.2 μ_B per atom. At 40 K, antiferromagnetic ordering Mn^{3+}/Mn^{4+} occurs; at $\sim$ 24 K, one deals with spin reorientation; and at 10 K, terbium ions undergo magnetic ordering (Fig. 1 *a*). A peak at 38 K in the temperature dependence of the dielectric constant (Fig. 1 *b*) along the axis *b* corresponds to a ferroelectric transition, which is due to a magnetic transition at about 40 K. The fact that no changes in ε along the axes *a* and *c* occur points that the electric polarisation (P) of the crystal is aligned to the axis *b*. It is assumed that the magnetic ordering of Mn^{3+}/Mn^{4+} 'induces' the ferroelectric transition by additionally distorting the crystal lattice in the vicinity of the Jahn–Teller ion Mn^{3+}, while the spin reorientation at 24 K is responsible for the step in the temperature dependence of ε. Note also that an increase in the heat capacity at temperatures below 10 K is due to magnetic ordering in the terbium sublattice.

The most interesting properties of this compound are due to the possibility of changing (switching) the direction of the electric polarisation of the crystal under the action of external magnetic field (Fig. 2). The magnetic field (B) was efficient only along the axis *a*. The sample was polarised along the axis *b* in a static electric field of 4 kV cm^{-1}. The dependence $\varepsilon(B)$ at 3 and 28 K (Fig. 2 *a*) shows maxima

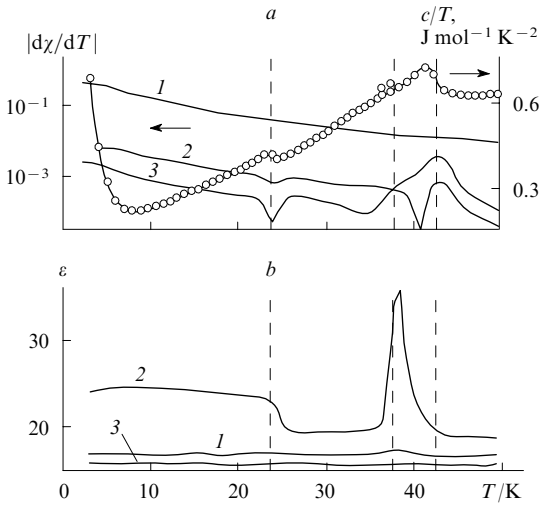


Figure 1. Changes in the dielectric and magnetic properties of $TbMn_2O_5$ upon phase transitions.[19]
The temperature derivative of the magnetic susceptibility (χ) along the crystallographic axes *a* (*1*), *b* (*2*) and *c* (*3*) and the heat capacity (c/T) plotted *vs*. temperature (*a*); the dielectric constant (ε) along the crystallographic axes plotted *vs*. temperature (*b*); 1 kHz a.c. heating.

near 1 T (with a small hysteresis); the magnetic field dependence of the polarisation $P(B)$ is shown in Fig. 2 *b*. The $\varepsilon(B)$ peak at 3 K weakens with an increase in temperature and disappears at 10 K, which can be explained by magnetic ordering in the terbium sublattice. Hysteresis in the $\varepsilon(B)$ plot at 28 K is responsible for the polarisation step (see Fig. 2 *b*). As the magnetic field increases from zero to 2 T, the polarisation P changes from +40 to −40 nC cm^{-2} (see Fig. 2 *b*). This occurs in a nonlinear fashion and seems to be consistent with the magnetic transition in the terbium system. Switching the polarisation direction can be

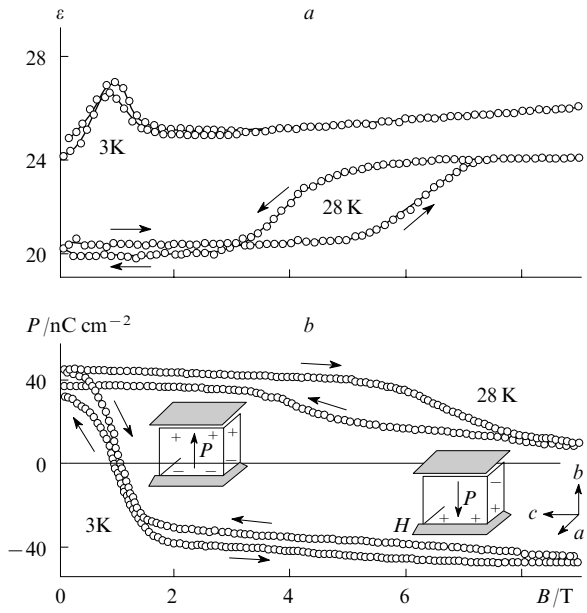


Figure 2. Magnetic field dependences of the polarisation of $TbMn_2O_5$ at 3 and 28 K.[19]

explained by the onset of ferrielectricity (analogously to the onset of ferrimagnetism), which ensures the total polarisation. In our case the total polarisation has a positive component, which spontaneously appears at the ferrielectric transition temperature ($\sim$38 K), and a negative low-temperature component below 24 K. The former component does not 'sense' external magnetic field while the magnitude of the latter component varies over a wide range, especially at temperatures near 15 K.

Noteworthy is yet another effect, which is related to the effect of magnetic field on the electric polarisation of the crystal. The case in point is the polarisation inversion, which occurs as the magnetic field slowly varies from 0 to 2 T. In this case well-reproducible non-damping oscillations are observed. This can be interpreted as polarisation menory, which is read by the magnetic field.

A multiferroic $BiFO_3$ with high ferroelectric and magnetic transition temperatures has been better studied than the compound mentioned above. The optimal properties of this compound manifest themselves in heterostructures and thin films.[20]

1. Heterogeneous multiferroics

The structure of $BiFeO_3$ includes two distorted perovskite unit cells that share a diagonal and thus form a rhombohedral lattice. The ferroelectric state appears due to a large displacement of bismuth ions relative to FeO_6 octahedra. Antiferromagnetic spin interaction appears between adjacent planes and acts normal to the electric polarisation vector. Whereas in the case of single-crystalline samples the electric polarisation is low, in the case of thin epitaxial layers a few nanometres thick it is rather high. The electric polarisation of $BiFeO_3$ films grown on $DyScO_3$ substrate (Fig. 3) is twice as high that of $TbMn_2O_5$ and the polarisation hysteresis curves are steep.

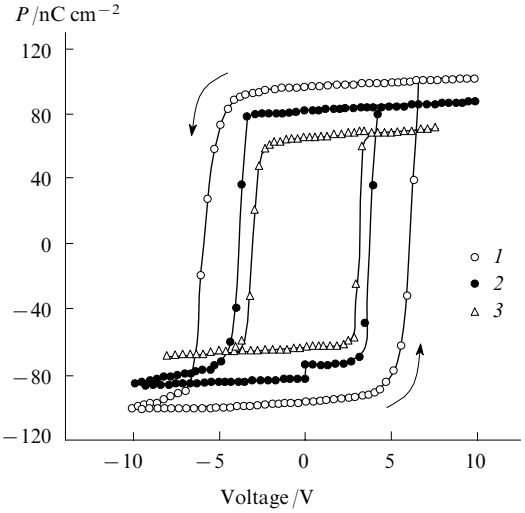


Figure 3. Ferroelectric polarisation hysteresis loops for $BiFeO_3$ epitaxial films grown on the (111) (*1*), (110) (*2*) and (100) (*3*) crystallographic planes.

The domain structure of ferroelectrics is studied by piezoelectric force spectroscopy, a technique similar to the magnetic force and atomic force microscopies. The domains with the 'up' and 'down' polarisation are 'seen' with different contrast. By applying an alternating voltage to the cantilever of a microscope one can change the direction of the polarisation vector of the system under study.

The antiferromagnetic structure of $BiFeO_3$ can be studied by photoemission electronic spectroscopy, which is based on linear magnetic dichroism of X-ray radiation.[21] The technique also allows the size of ferroelectric domains to be controlled. The temperature dependences obtained for $BiFeO_3$ films revealed the existence of antiferromagnetic and ferroelectric domains in these systems. Since there is an interplay between the ferroelectric and antiferromagnetic sublattices of the $BiFeO_3$ epitaxial films, fine control of magnetism can be attained by varying an external electric field.

Since $BiFeO_3$ is mainly used in the form of epitaxial nanofilms, one should pay attention to the effect of mechanical strain, which appears during the film growth on various substrates. Theoretical calculations showed that the ferroelectric polarisation is almost 'insensitive' to the lattice strain,[22] but this strain can violate the magnetic symmetry and thus change the plane of rotation of the polarisation vector;[23] *i.e.*, additional possibilities of controlling the changes in the magneto-electric coupling appear. At present, a technology of coating the $SrTiO_3$, $DyScO_3$ and $LaAlO_3$ substrates as well as the $SrRuO_3$, $(La,Sr)MnO_3$ and $LaNiO_3$ conducting electrodes with $BiFeO_3$ epitaxial films has been elaborated. By varying the substrate material and the $BiFeO_3$ film thickness one can control the strain-induced effects. Changes in the lattice constant normal to the plane of $BiFeO_3$ films grown on $SrTiO_3$ and $DyScO_3$ substrates are illustrated in Fig. 4. Owing to mismatch of the lattice parameters of $SrTiO_3$ and $BiFeO_3$ the $BiFeO_3$ film is compressed in the horizontal plane and stretched in the vertical plane; the mechanical strain decreases as the film thickness increases. The maximum strain is attained at a film thickness of about 30 nm. The lattice constants of the $DyScO_3$ substrate and the $BiFeO_3$ film match one another; therefore, the strain is independent of film thickness.

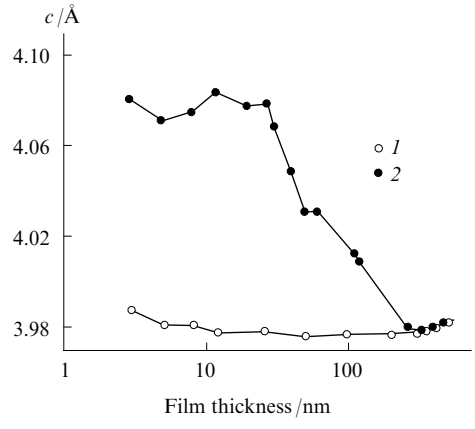


Figure 4. Lattice constant along the normal to the film plane plotted *vs*. film thickness for $BiFeO_3$ films grown on $SrTiO_3$ (*1*) and $DyScO_3$ (*2*) substrates.[20]

Not only epitaxial multiferroic films on various substrates, but also self-organising multiferroic wires oriented normal to the substrate surface can be prepared. These wires ensure magneto-electric coupling in the system.[24] To this end, a perovskite-type ferroelectric $BaTiO_3$ and spinel-

type $CoFe_2O_4$ were used. In both cases, the lattice constant was $\sim 4(0.2)$ Å, thus providing three-dimensional epitaxy and sufficiently strong magneto-electric coupling. A $BaTiO_3-CoFe_2O_4$ nanostructure was formed by laser deposition on $BaTiO_3$ substrate coated on $SrRuO_3$ electrode. The nanostructure was studied by X-ray scattering, atomic force microscopy (AFM) and transmission electron microscopy (TEM). Scanning over the X-ray scattering angle revealed a high degree of crystallinity of the oriented nanostructure. An almost periodic structure (AFM data) is comprised of hexagonal (TEM data) $CoFe_2O_4$ columns (20–30 nm in diameter) in the $BaTiO_3$ matrix (Fig. 5). The lattice constants are $a = b = 3.99$ and $c = 4.04$ Å for $BaTiO_3$ and $a = b = 8.38$ and $c = 8.31$ Å for $CoFe_2O_4$. The $CoFe_2O_4$ nanocolumns are somewhat compressed (by 0.8%) due to the epitaxial mismatch of the $CoFe_2O_4$ and $BaTiO_3$ lattices. Ferroelectric measurements showed the polarisation hysteresis (Fig. 6*a*) with a saturation of 23 μC cm^{-2} and a piezoelectric displacement of ~ 50 pm V^{-1} (*cf.* 130 pm V^{-1} for $BaTiO_3$ single crystal).

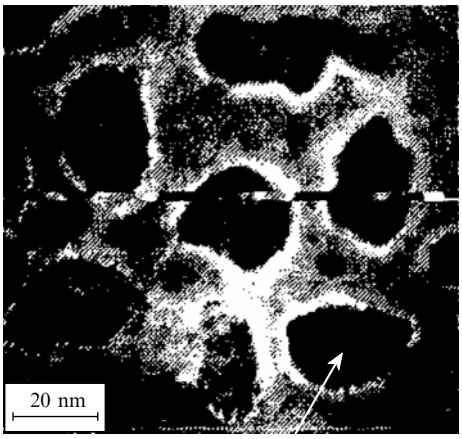


Figure 5. TEM image of $CoFe_2O_4$ nanocolumns (white arrow denotes a single column) in $BaTiO_3$.[24]

Based on the data obtained using superconducting quantum interference devices (SQUIDs), the saturation magnetisation was estimated at a value of ~ 350 (emu) cm^{-3}; a high anisotropy of ~ 3.5 T between the directions (001) and (100) was also revealed. Comparison of this value with the result of calculations (0.21 T)[24] suggests a strong effect of mechanical strain on the $CoFe_2O_4$ nanocolumns in the $BaTiO_3$ matrix, which is due to the mismatch of the crystal lattice parameters. Compressing strain of $CoFe_2O_4$ can induce magnetic anisotropy (owing to magnetostriction). Compression of the $CoFe_2O_4$ lattice can be described as follows:

$$\sigma_{001} = A\varepsilon_{001},$$

where the strain along the (001) axis is proportional to the atomic displacement and the elastic modulus (Young modulus) is $A = 141.6$ GPa. The magnetoelastic energy is given by

$$e = -\frac{3\lambda_{001}\sigma_{001}}{2},$$

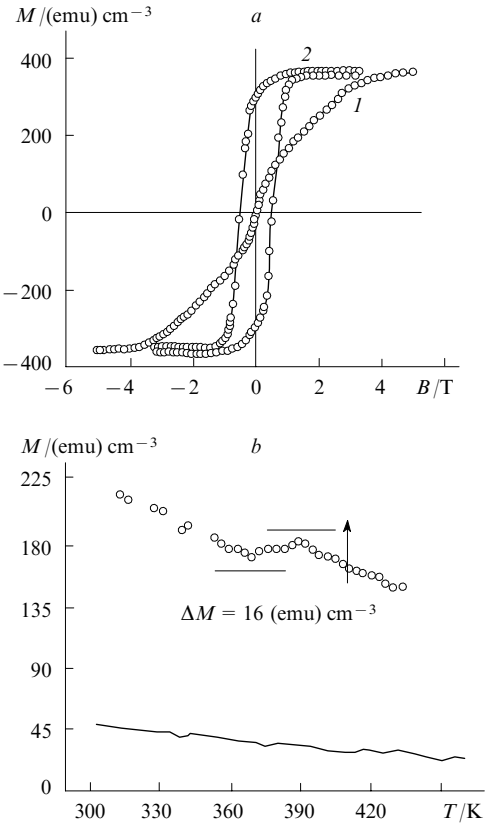


Figure 6. Magnetic field dependences of the normal (*1*) and in-plane (*2*) magnetisation (M) components (*a*) and the temperature dependence of the magnetisation (B = 100^{-2} T) for a $BaTiO_3-CoFe_2O_4$ (substrate) nanostructure; the lower curve was obtained for multilayer epitaxy (*b*).[24]

where λ_{001} is the magnetostriction coefficient of $CoFe_2O_4$ ($\sim -350\times10^{-6}$, see Ref. 25). The magnetoelastic energy is 5.95×10^6 erg cm^{-3} and the magnetic anisotropy is 3.4 T, which is comparable with experimental data.

The temperature dependence of the magnetisation of the $BaTiO_3-CoFe_2O_4$ nanostructure (see Fig. 6*b*) suggests a strong coupling between the electric and magnetic components. This follows from the decrease in the magnetisation near the ferroelectric transition temperature (~ 290 K). At $T > T_C$, the $CoFe_2O_4$ nanocolumn is compressed due to the mismatch with the lattice parameters of $BaTiO_3$. At $T < T_C$, tetragonal distortion of the $BaTiO_3$ lattice to some extent levels this compression. Owing to negative magnetostriction of $CoFe_2O_4$, the magnetisation of the system decreases. Changes in the magnetisation near T_C can be estimated from the relation

$$\frac{\Delta M}{M} \approx \frac{QP^2E(\mathrm{d}\lambda/\mathrm{d}M)}{M},$$

where Q is the electrostriction coefficient and P is the electric polarisation.[24]

2. Devices implementing multiferroics

Both direct (ME) and reverse (EM) magnetoelectric effect can occur in multiferroics. The former effect is accompanied by magnetically induced changes in the electric polarisation (or potential), while the latter effect is accompanied by the

changes in magnetisation induced by the electric field E. In free systems (no coupling between the magnetic and electric systems), the direct and reverse effects are equivalent and characterised by equal coefficients

$$\alpha = \left(\frac{\partial P}{\partial H}\right)_E = \mu_0 \left(\frac{\partial M}{\partial E}\right)_B,$$

where H is the magnetic field strength and μ_0 is the magnetic permittivity of vacuum. Enhancement of the EM-effect compared to the ME-effect can be used in memory devices, where information is written electrically (by changing the ferroelectric characteristics) while fast and nondestructive readout is done by changing the magnetisation. The best results in this field were obtained using multiferroid nanostructures, which include manganite nanofilms ensuring the magnetic interaction and a ferroelectric, which is responsible for mechanical strain of the epitaxial surface.

Magnetic ordering is highly sensitive to the bond lengths and bond angles (especially, in d-element oxides). Manganites (Ln,A)MnO_3 (Ln is the rare-earth element and A is the dopant, *e.g.*, Ca, Mg, Sr) are quite sensitive to changes in magnetisation. These materials exhibit the giant magnetoresistance effect under the action of external pressure and epitaxial strain.[26,27] The second component of a multiferroic can be a piezoelectric, *e.g.*, $PbTiO_3$, $BaTiO_3$, $SrTiO_3$, *etc.*

The effect of epitaxial strain on the magnetisation and magneto-electric effect in $La_{0.7}A_{0.3}MnO_3$/PMNT [A = Sr, Ca; PMNT = $Pb(Mg_{1/3}Nb_{2/3})_{0.72}Ti_{0.28}O_3$] nanostructures has been studied.[28]

$La_{0.7}A_{0.3}MnO_3$ epitaxial films 20–50 nm thick were grown by laser deposition on a single-crystalline surface of a PMNT plate.

Studies of the magnetisation and residual magnetisation of the manganite films grown on the PMNT surface showed a noticeable increase in magnetisation (to 25%) at 330 K and $E = 10$ kV cm^{-1}. The residual magnetisation can also vary and be controlled. It should be noted that the magnetisation hysteresis was observed up to the maximum electric fields, whereas for the ferroelectric substrate the strain hysteresis was observed only up to 2 kV cm^{-1}. This suggests the influence of magnetic domains on the magnetic hysteresis. The increase in mechanical strain was attributed to the increase in the manganite T_C values due to piezoelectric compression and to a possible effect of changes in the magnetic anisotropy.

Direct control of the magnetisation of a nanostructure using changes in mechanical strain can be practically valuable for tuning of permanent magnets or changing their magnetisation. The coupling constant of these films ($\alpha \approx 6 \times 10^{-8}$ S m^{-1}) is higher than those of many single-phase materials.[29]

Stronger magneto-electric coupling was observed in 40-nm $La_{0.67}Sr_{0.33}MnO_3$ epitaxial films grown on the surface of $BaTiO_3$ plates 0.5 mm thick ($BaTiO_3$ is a typical ferroelectric). At room temperature, $BaTiO_3$ has a tetragonal unit cell with the lattice constants $a = b = 3.99$ and $c = 4.03$ Å. At high temperatures, $BaTiO_3$ has a non-ferroelectric cubic structure (C); but undergoes transition to the tetragonal phase (T) on cooling below $T_C = 410$ K. This is followed by transitions to the orthorhombic phase (O) below 290 K and the rhombohedral phase (R) below 190 K. The oxide $La_{0.67}Sr_{0.33}MnO_3$ has a perovskite-type structure with a pseudocubic lattice (lattice constant $a = 3.87$ Å). Bulk material exhibits the properties of a ferromagnetic below 365 K, the transition temperature T_C being sensitive to the epitaxial and boundary mechanical strain.[30]

Five film samples were prepared by laser deposition.[31]

The results of studies of the temperature dependence of magnetisation are shown in Fig. 7. A noticeable jump-like decrease in the magnetisation near the R → O phase transition is clearly seen. Further heating of the sample causes the magnetisation to decrease down to vanishing near the Curie temperature. These measurements provided a clear

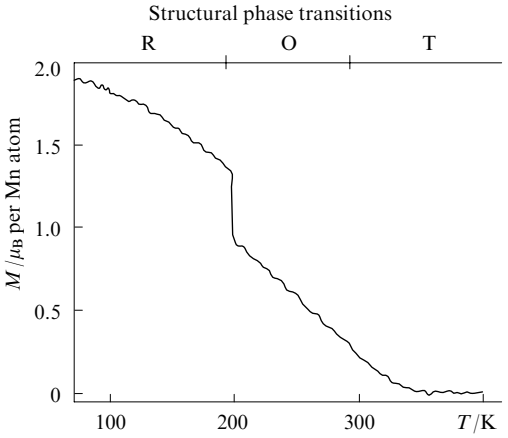


Figure 7. Magnetisation-*vs.*-temperature plot for $La_{0.67}Sr_{0.33}MnO_3$ epitaxial film grown on $BaTiO_3$ substrate.[31]

illustration of the effect of the phase transitions of $BaTiO_3$ on the magnetisation of the $La_{0.67}Sr_{0.33}MnO_3$ epitaxial film. Figure 8 presents the key results for three different samples. These data were obtained by monitoring the magnetic response of the sample to the potential difference between the film and substrate surfaces. As the potential difference increases, the magnetisation of the film initially remains unchanged. A remarkable result obtained in this study[31]

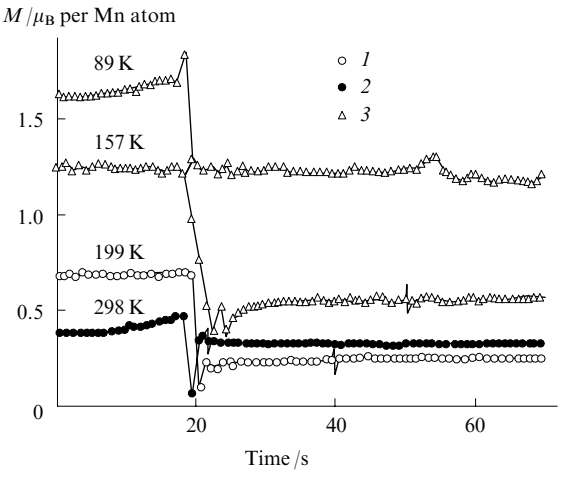


Figure 8. Electrically induced magnetic changes at different temperatures.[31]
'Switching' time (20 s) was chosen for a potential of 4 (*1*), 10 (*2*) and 6 kV (*3*).
Sample No.: 3 (*1*), 4 (*2*) and 5 (*3*).

consists in the observation of a large and constant magnetisation jump upon attainment of a certain threshold potential. As the potential further increases (or is 'switched off'), the magnetisation also remains unchanged. The rate of change in the magnetisation is limited by the rate of ferroelectric switching at about 10^{-8} s. If the metering equipment is characterised by a temporal resolution of ~ 1 s, the actual switching time (see Fig. 8) is determined by specific features of the equipment. This nanosystem has the record high coupling constant ($\alpha = 2.3 \times 10^{-7}$ S m^{-1}), which is due to the R $\rightarrow$ O phase transitions in the ferroelectric and to an increase in the mobility of the polarisation domain boundaries, and to the spontaneous magnetisation of $La_{0.67}Sr_{0.33}MnO_3$. The coupling constant α near room temperature and in the case of the O $\rightarrow$ T transition was 2.3×10^{-8} S m^{-1}, which approaches the published data (see, *e.g.*, Ref. 32).

Magnetic information can be deleted by applying a magnetic field of 8 T to the sample under study at 470 K; in this case $BaTiO_3$ has the cubic structure.

III. Spintronics

The spintronics include materials in which magnetically- or electrically-induced, spin-dependent electric current can flow. Here, the 'spin' means the spin of an atom, a nanocluster or a domain. In 1988, studies of spintronic materials led to the discovery of the effect of giant magnetoresistance in metallic multilayers,[33] which was accompanied by considerable (tens of per cent) decrease in electrical resistance of the sample in external magnetic field. Since then, intensive research has been carried out in this field of materials science.† This effect is called differently in the literature, *e.g.*, the giant magnetoresistance and the colossal magnetoresistance. However, due to a large scatter of magnetically-induced changes in the resistance it is appropriate to use the term 'magnetoresistance'. Prior to considering the spintronics and devices based on them, one should consider systems and compounds for which the magnetoresistance phenomenon is observed and the mechanisms of the onset of magnetoresistance.

1. The magnetoresistance

The magnetoresistance (MR) effect consists in a significant decrease (to 1000%) in the electrical resistance of a nanomaterial in external magnetic field; the resistance of bulk samples under identical conditions changes insignificantly [*e.g.*, the resistance of permalloy (80% Ni + 20% Fe) increases by 3% in a magnetic field]. The MR effect was observed in studies of the magnetic properties of various metallic and oxide nanosystems. The mechanisms of the onset of the MR effect in nanocrystalline metals and metal oxides are different.

Nanocluster metallic materials exhibiting the MR effect are prepared by dissolving metal (*e.g.*, Fe or Co) nanoclusters in a conducting metal (*e.g.*, Cu or Ag) matrix provided a poor mutual solubility of the components of the material being prepared. If the nanosystem comprises a conducting metallic matrix and magnetic clusters incorporated into this matrix, the conduction electrons of the metallic matrix are scattered by the magnetic moments of the clusters. The clusters are rather small and can show the properties of superparamagnetics. However, since the conduction electrons move at the Fermi velocity, the magnetic moments of the clusters are 'blocked' because the time taken by the magnetisation measurements (~ 100 s) is much longer than the time taken by an electron to pass through the sample ($\sim 10^{-9}$ s). The MR effect is observed even at the temperatures corresponding to zero residual magnetisation or zero residual magnetic moment. The electronic structure of the metallic matrix has little effect on the properties of magnetic clusters.[34]

Electron scattering on the magnetic moments of clusters in metals occurs faster than their spin orientations are changed, but the relative orientations of the magnetic moments of clusters affect the scattering rate and, correspondingly, the conductivity. Namely, as the orientations of the magnetic moments of clusters change under the action of external magnetic field, they begin to interact with the conduction electrons; as a consequence, the conductivity changes. The magnitude and the MR phenomenon itself are determined by the ratio of the free path length of an electron and the distance between neighbouring magnetic clusters, which depends on the concentration of nanoclusters in the matrix. At low metal concentration in the matrix and, correspondingly, long free path length of an electron the electron participates in numerous acts of scattering before the onset of the interaction with the magnetic cluster. In this case the orientation of the magnetic moment of the cluster has no effect on electron scattering and no MR effect occurs. At high concentration of clusters, they interact with one another and participate in percolation processes, which also causes the MR to vanish. For the nanosystem Co$-$Ag, the MR effect manifests itself as the cobalt concentration changes from 15% to 40%.[34] The maximum effect was observed at a cobalt concentration of about 20%, which was associated with the optimal size of cobalt clusters in the silver matrix. The effect becomes more pronounced as the temperature is lowered.

It is interesting to study the dependence of the magnetoresistance on the magnetic field normalised to the MR saturation magnetisation,

$$|MR| = \left|\frac{\rho_B - \rho_0}{\rho_0}\right| \approx \left(\frac{M}{M_s}\right)^2, \quad (1)$$

where ρ_B is the film resistance in magnetic field, ρ_0 is the film resistance in zero field and M_s is the saturation magnetisation. If a nanosystem exhibits the MR effect, each magnetic cluster participates in spin-dependent electron scattering; therefore, the MR effect should be influenced by cluster$-$cluster interactions. Experiments give the total magnetoresistance due to the total change in the magnetisation.[34] However, the cluster size distribution and cluster$-$cluster interactions lead to changes in relation (1).

The MR effect can be considered using the two-current model, according to which the 'up' and 'down' electron scattering on the magnetic moment of a cluster in a disordered nanosystem is equivalent. In the magnetically ordered nanosystem, the resistance along the magnetic field direction is lower than in the opposite direction; this leads to a decrease in the total resistance.

The decrease in MR ($\Delta\rho$) correlates with the increase in the cluster size (d)

$$\Delta\rho \sim \frac{1}{d}.$$

† In 1998, IBM Corp. began production of devices whose operation is based on this effect.

This shows that the MR ratio is determined by the ratio of the surface area of magnetic clusters and the surface area of interfaces to their volume and suggests that spin-dependent electron scattering does occur at the cluster/matrix interfaces.

Perovskite-type manganites are characterised by even more pronounced MR effect. These are ceramic materials to which the cluster models proposed for the previously studied nanosystems can be applied. As an example, we will consider the MR effect in $La_{0.67}Ca_{0.33}MnO_x$ films grown on $LaAlO_3$ substrate.[35] The films 100–200 nm thick were prepared by laser epitaxial deposition of the components of the La–Ca–Mn–O system on the substrate and heating in oxygen atmosphere. Magnetoresistance measurements were performed with the 100-nm-thick films in magnetic fields of up to 6 T. In most cases, the magnetic field direction was parallel to that of electric current (experiments showed that the MR is independent of the magnetic field direction).

The results of studies on the magnetically induced relative changes in the electrical resistance and on the changes in the magnetisation of the sample in a 6-T magnetic field are shown in Fig. 9. The maximum MR effect is observed at $B = 4–6$ T and $T \approx 190$ K, *i.e.*, near the transition to the metallic state. At the same time, analysis of the dependence of the magnetic moment of manganite revealed no magnetic phase transition in the temperature interval 190–220 K and a smooth decrease in the magnetisation from the maximum value [saturation magnetisation, about 300 (emu) cm^{-3}] to 100 (emu) cm^{-3}. Therefore, it is the semiconductor–metal phase transition rather than magnetic phase transition that is mainly responsible for the onset of the MR effect.

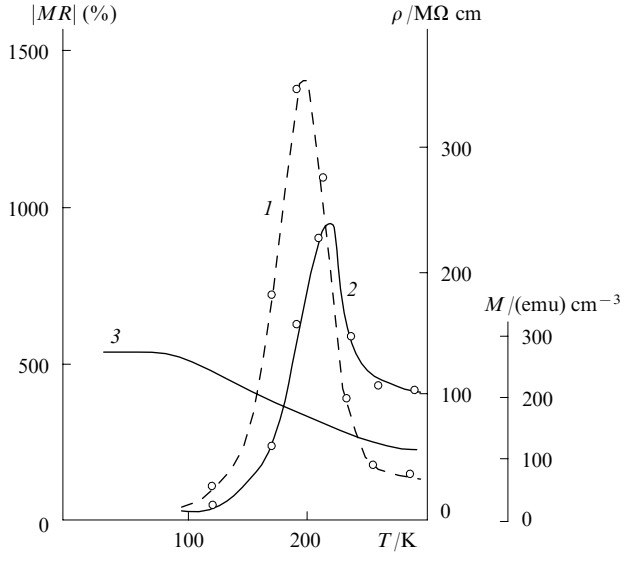


Figure 9. Temperature dependences of the MR ratio (*1*), ρ (*2*) and M (*3*) for $La_{0.67}Ca_{0.33}MnO_x$ ceramics.[35]

The MR ratio is sensitive to the annealing temperature and oxygen concentration. In particular, the MR measurements for a film grown at 640 °C gave a diffuse peak with a maximum $|MR| = 500\%$ at 100 K; the film annealed at 700°C in oxygen atmosphere for 30 min was characterised by a peak $|MR| = 1400\%$ at ~200 K; further increase in the annealing temperature to 900 °C led to shift of the maximum of the $|MR|$ ratio towards 280 °C.

The mechanism of the onset of the MR effect in ceramics seems to be different compared to metals. Here, the Mössbauer spectroscopy appeared to be an efficient method of investigation. $La_xCa_{1-x}Mn_2O_3$ manganites with partial replacement of manganese atoms by iron atoms were studied.[36] The Mössbauer spectra of the manganite $La_{0.75}Ca_{0.25}Mn_{0.98}Fe_{0.02}O_3$ prepared by sintering metal oxides and salts at different temperatures are shown in Fig. 10.

A characteristic feature of these spectra is their resolution in the MR region into a central paramagnetic (super-

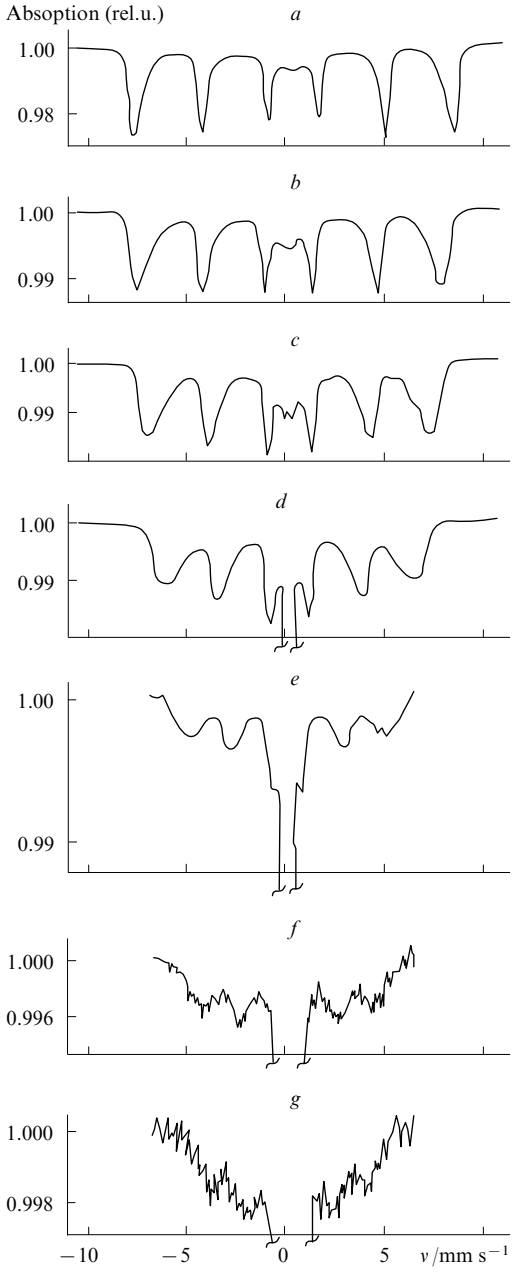


Figure 10. Mössbauer spectra of $La_{0.75}Ca_{0.25}Mn_{0.98}Fe_{0.02}O_3$ ceramics at 78 (*a*), 100 (*b*), 120 (*c*), 150 (*d*), 185 (*e*), 200 (*f*) and 210 K (*g*).[36] Here and in other Mössbauer spectra v is the velocity of the radiative source relative to the absorber.

paramagnetic) doublet and a magnetic hyperfine structure (HFS). Line broadening observed on heating from 150 to 200 °C indicates a relaxation behaviour of the magnetic moment, which is similar to superparamagnetism of cluster nanosystems. To a first glance, this is not related to the ceramic state of the sample comprised of coarse grains prepared by high-temperature sintering of the starting components. Inelastic neutron scattering data disclose the appearance (at low temperatures) of a spectral component, which dominates as the ferromagnetic (metallic) – paramagnetic (semiconductor) transition temperature of the ceramics is approached (T_C = 250 K).[37]

Taking account of these results, one can assume that the MR in the region of the semiconductor – metal transition of the ceramics is due to the appearance of fluctuating, ferromagnetically ordered nanosize domains. The size of such domains increases as the temperature decreases. Broadening of the region of the semiconductor – metal transition of the ceramics is accompanied by an increase in the superparamagnetic relaxation time and eventual transition to the magnetically ordered ferromagnetic state. The temperature interval corresponding to this magnetic transition can span a few tens of degrees, but it is this temperature interval that is responsible for the change in the scattering of conduction electrons and the onset of the MR effect due to the changes in the relaxation time of the magnetic moment, in the distances between fluctuating clusters and in the cluster size. This can be explained by the fact that no ferromagnetic nanoblocks are formed at temperatures below the phase transition temperature and by the lack of metallic conductivity at high temperatures.

2. Phase separation in manganites

The conductivity of spintronic materials can be controlled not only magnetically, but also electrically. As examples, we will again dwell on manganites.[38]

The phase diagram of $Re_{1-x}A_xMnO_3$ compounds (A is an ion of, for example, an alkaline earth element) characterises three states [ferromagnetic metallic, antiferromagnetic semiconductor (or dielectric) and paramagnetic semiconductor state] and includes regions (depending on the nature and content of the alkaline earth metal). Since the Mn^{3+} ion belongs to Jahn – Teller systems, structural distortion of the oxygen octahedron surrounding the Mn^{3+} ion induces a strong interaction between the electronic system and the crystal lattice. The electronic and magnetic properties of this manganite are closely related to transfer of 3d-electrons from Mn^{3+} to $Mn^{(3+/4+)}$ involving O2p-electrons. Changes in the bond angles and bond lengths cause significant changes in the exchange integral (J)

$$J \approx \frac{\cos(\theta/2)\cos\psi}{d^{5/2}}, \qquad (2)$$

where θ is the angle between the spin orientations, ψ is the covalent bond angle and d is the bond length.

Therefore, lattice distortions and strain play a significant role in determining the properties of matter, *viz.*, they induce phase transitions responsible for the magnetic and electric properties of manganites; in particular, they can depend on the film thickness and temperature.[39]

Theoretical models (see, *e.g.*, Ref. 40) predict co-existence of phases with different electron densities and structural distortions. The formation of different phases relieves mechanical strain. The dimensions of the manganite phases can vary from 1 to 10^3 nm. Phase separation is thought to be common to complex oxides and used to explain various properties of these compounds.

One can monitor separation of the magnetic conducting and charge insulating phases near the transition temperature using, *e.g.*, a scanning tunnelling electron microscope.[41] However, the possibility of observation is often determined by the sample preparation procedure and the experimental design and methodology.[42]

Phase separation can also be monitored using magnetic force microscopy, here the magnetic phase of the $(La,Pr,Ca)MnO_3$ film changes with temperature.[43] A single-crystalline sample revealed separation of the magnetic conducting and the polarised non-conducting phases.[44] In addition, a correlation was established between the changes in the magnetic phase and the twin boundaries; this is due to the effect of the crystal structure on the magnetic properties.

The existence of individual phases in manganites opens prospects for the design of electric or magnetic memory devices.[45] Applying weak magnetic fields causes significant changes in phase separation; if the magnetic field acts for a short time, abrupt switching occurs.

3. Devices based on spintronic materials

Manganite thin films are used in various devices including, *e.g.*, storage devices, magnetic sensors, transistors, *etc.*[46] Earlier, this type of devices used manganite thin-film junction arrays (two manganite electrodes separated by an insulator), which ensured magnetic quantum transitions.[47] The magnetotransport properties of this junction array changed depending on the orientation of the magnetic moments of the electrodes. The magnetoresistance effects should manifest themselves in weak external magnetic fields. This is attained using the structure in which the exchange interactions between paired manganite electrodes vanish under the action of a weak magnetic field comparable with the coercive force of the material. The conductivity due to the electrons with particular spin orientation will depend on the mutual orientation of the electrodes.

The three-layer columnar nanostructure was prepared using $La_{0.67}Ca_{0.33}MnO_3$ (LCMO) or $La_{0.67}Sr_{0.33}MnO_3$ (LSMO) layers and a thin $SrTiO_3$ (STO) layer. Films were grown by laser deposition. The nanoscale junction array comprised the basal LCMO (or LSMO) layer ~60 nm thick and an upper LCMO (or LSMO) layer ~40 nm thick separated by a ~5-nm STO layer. Measurements of the magnetic properties of these junction arrays revealed the maximum coercive force (~0.03 T) at low temperatures.

Based on the results of MR measurements, the magnetic field dependence of MR on lowering the temperature starting at ~200 K was established. At 4.2 K, the MR was doubled. This is a consequence of spin-dependent electron transfer through the barrier (STO layer). The tunnelling conductivity (through the STO layer) depends on the mutual arrangement of domains within the LSMO layers. A change in the domain configuration of an electrode relative to the other one causes the overall conductivity to change. The range of magnetic fields appropriate for switching is of the order of 10^{-2} T.

The magnetoresistance can be further increased by choosing and improving the quality of the boundary layers and by reducing the charge transfer between the layers. The tunnelling magnetoresistance (TMR) increases by 50% for the LSMO/STO/LSMO junction array, by 170% for the LSMO/LMO/STO/LMO/LSMO junction array, where

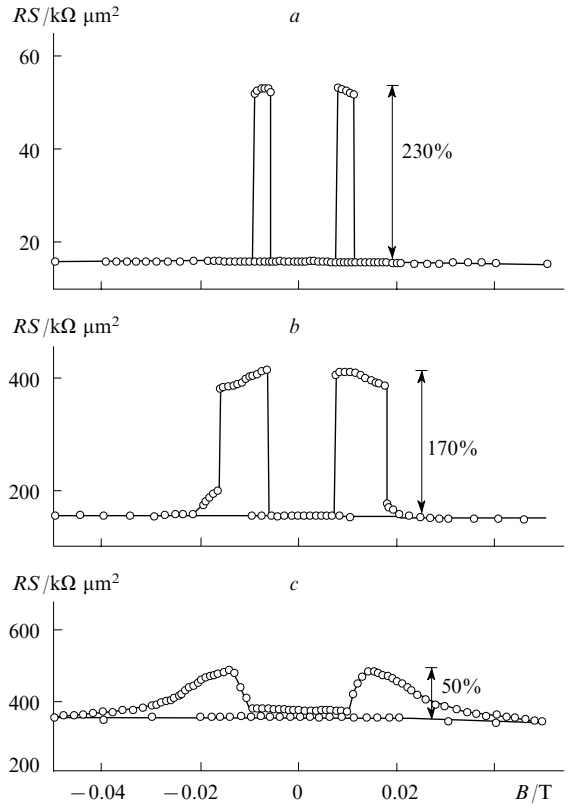


Figure 11. Tunnelling magnetoresistance of nanostructures LSMO/STO/LSMO (*a*), LSMO/LMO/STO/LMO/LSMO (*b*) and LSMO/LAO/LSMO (*c*) plotted *vs.* magnetic field; $T = 10$ K.[48]
S is the surface area of the nanostructure.

LMO = $LaMnO_3$ and by 230% for the LSMO/LAO/LSMO junction array, where LAO = $LaAlO_3$ (Fig. 11).[48]

The tunnelling magnetoresistance is the key notion in the studies on fabrication of memory devices, magnetic sensors and programmable logic gates in electronic devices.[49–51] The tunnelling magnetoresistance (R) is defined by the ratio

$$R = \frac{R_{ap} - R_p}{R_p},$$

where R_p and R_{ap} are the tunnelling resistances at parallel and antiparallel magnetisations of the basal and upper electrodes, respectively. Theoretical models predict a high TMR for the Fe/MgO/Fe junction array.[52] High tunnelling probability is ensured by coherent electron wave functions, which are symmetric with respect to the normal to the intermediate (barrier) layer and do not change in the course of tunnelling transition.

The TMR of epitaxial nanoscale junction array Fe/MgO/Fe was studied; here the thickness of the MgO barrier was varied from 1.2 to 3.2 nm (epitaxial films were fabricated using the molecular beam technique).[53] The magnetoresistance at 1300 mV was measured at 20 and 293 K. Room-temperature measurements revealed a remarkable result, *viz.*, TMR $\sim$180%.

Analysis of the dependence of the *RS* value on the film thickness suggests the mechanism of this effect. TMR should increase with the thickness of the MgO barrier layer because of (i) smaller deviation of the vector characterising electron transfer from the normal to the barrier and (ii) weaker electron scattering.[54] Experiments showed an increase in the parameter *MR* and its oscillations with a period of 0.3 nm (Fig. 12). These oscillations are not a consequence of epitaxial buildup of the MgO layer, because the MgO monolayer is 0.22 nm thick. Probably, coherent tunnelling through the MgO barrier is due to interference between two electronic states of the iron atom with the corresponding basis vectors.

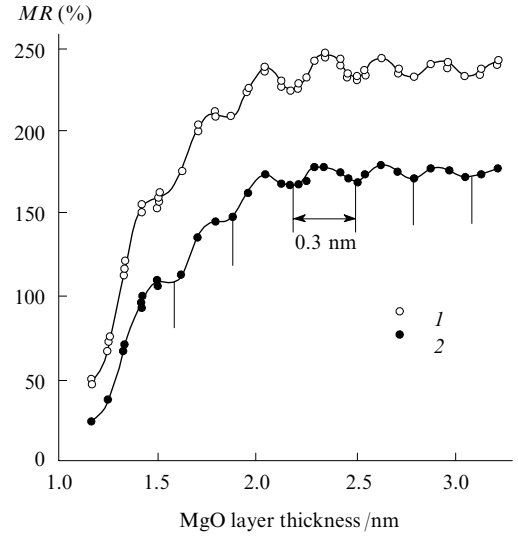


Figure 12. *MR* ratio plotted *vs.* thickness of MgO layer; $T = 293$ (*1*) and 20 K (*2*).[53]

Spin-polarised tunnelling responsible for quantum mechanical correlation between the wave functions of two electrodes can become a new 'tool', which will find application in the design of devices based on spintronic materials.

Organic compounds are also used in the design of tunnelling nanostructures as barrier materials to separate manganite layers. Here, the barrier layer can be much thicker than in the case of inorganic oxides. It is believed that carbon atoms are characterised by weak spin–orbit coupling; this ensures conservation of the electron spin polarisation in the course of tunnelling and thus primary magnetic information. For instance, submicrometre 8-hydroxyquinolylaluminium (Alq_3) layers between the $(La,Sr)MnO_3$ and Co electrodes showed a low-field TMR of $\sim$ 30%.

Of course, it is interesting to test carbon nanotubes as tunnelling barrier because the nanotube conductivity can be controlled from the semiconductor to metal conductivity. Such a nanostructure comprising two $La_{0.7}Sr_{0.3}MnO_3$ electrodes connected by a multiwalled carbon nanotube 20 nm in diameter and more than 1 μm long was synthesised and successfully tested.[55] A remarkable result consists in conservation of the magnetic spin polarisation on tunnelling despite the very long distance; the TMR parameter is 61%. In Fig. 13 the *MR* ratio and the electrical resistance at 5 K are plotted *vs.* magnetic field for different orientationns of the magnetic field and the electrodes. These dependences are used in the design of novel devices based on spintronic materials, *e.g.*, carbon nanotube spin transistors.

Multiferroics and spintronics can be implemented in a single material and a single device.[56] $La_{0.1}Bi_{0.9}MnO_3$

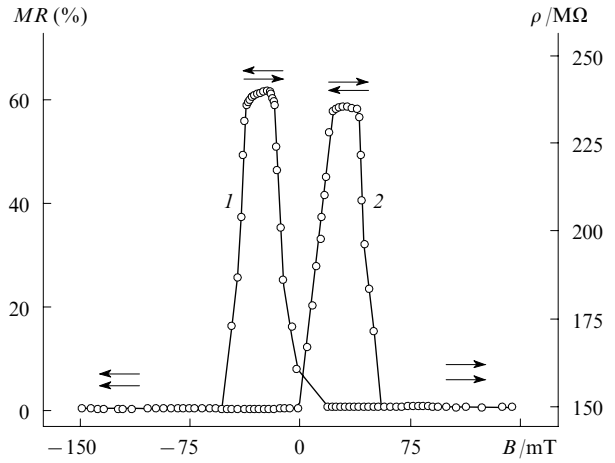


Figure 13. *MR* ratio and the electrical resistance of a nanostructure comprising two $La_{0.7}Sr_{0.3}MnO_3$ electrodes (*1*, *2*) connected by a carbon nanotube plotted *vs*. magnetic field ($T = 5$ K).[55]
Asterisks denote the orientation of the electrodes relative to the magnetic field direction.

(LBMO) thin epitaxial films (up to 2 nm thick) coated on $La_{2/3}Sr_{1/3}MnO_3$ (LSMO) exhibited both ferromagnetic and ferroelectric properties. This predetermined their use as tunnelling (Schottky) barriers in systems with electrically induced magnetic tunnelling transitions. Such systems can be called spin filters in which the barrier height depends on the orientation of electron spin, because the lowest energy level in the conduction band is split due to exchange interaction. This allows one to induce a spin-polarised current, which is highly sensitive to TMR provided that one electrode is ferromagnetic. Figure 14 presents the schemes of the tunnelling potential barriers and the tunnelling electron current for ferromagnetic and ferroelectric barriers in a LBMO/LSMO/Au junction array (Fig. 14 *a*), where Φ_0 is the barrier height in the case of no ferromagnetism, $\Delta\Phi_{ex}$ is the energy of exchange interaction, the 'spin-up' electrons from the LSMO layer are characterised by a lower potential barrier ($\Phi_0 - \Delta\Phi_{ex}/2$), higher current density (I) and lower resistance. In the case of antiparallel spins the barrier increases to ($\Phi_0 + \Delta\Phi_{ex}/2$) and the current density decreases. The tunnelling current is modulated due to ferroelectric polarisation of the LBMO barrier (Fig. 14 *b*), where Φ_0 is the barrier height in the case of no polarisation and Φ_+ and Φ_- are the barrier heights for the corresponding orientation of the polarisation P. Thus, this transition defines four states of the nanostructure, four tunnelling currents and four values of the electrical resistance of this device.

Multiferroid character of spintronic materials was studied taking LBMO films 2-40 nm thick as substrate, LSMO films 30 nm thick as lower electrode and an Au layer as the upper electrode. Figure 15 illustrates four states of the LSMO/LBMO/Au nanostructure at different orientations of the magnetisation of the barrier (dashed arrows) and the polarisation (solid arrows). It also presents the magnetic field dependences of the TMR of the

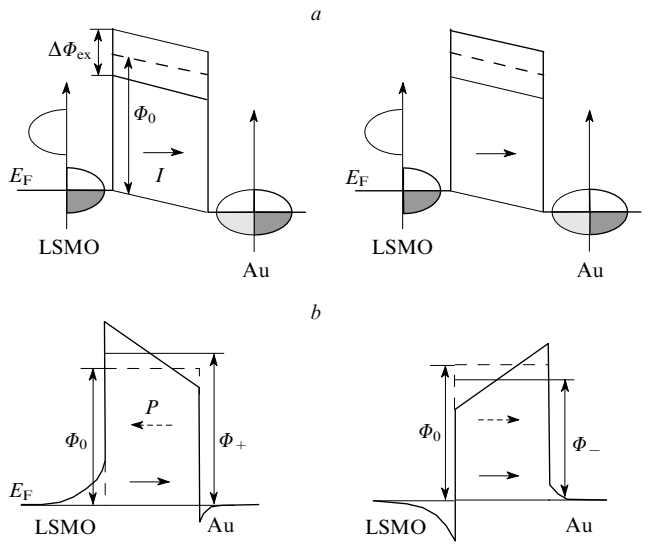


Figure 14. Schematic of magnetically (*a*) and electrically (*b*) induced tunnel electron transfer through potential barriers in LSMO/LBMO/Au junctions.
Shown are the populations of the conduction bands of the Au layers and the Fermi level positions (E_F). Characteristic of the LSMO is the up-spin semimetal state (see text).

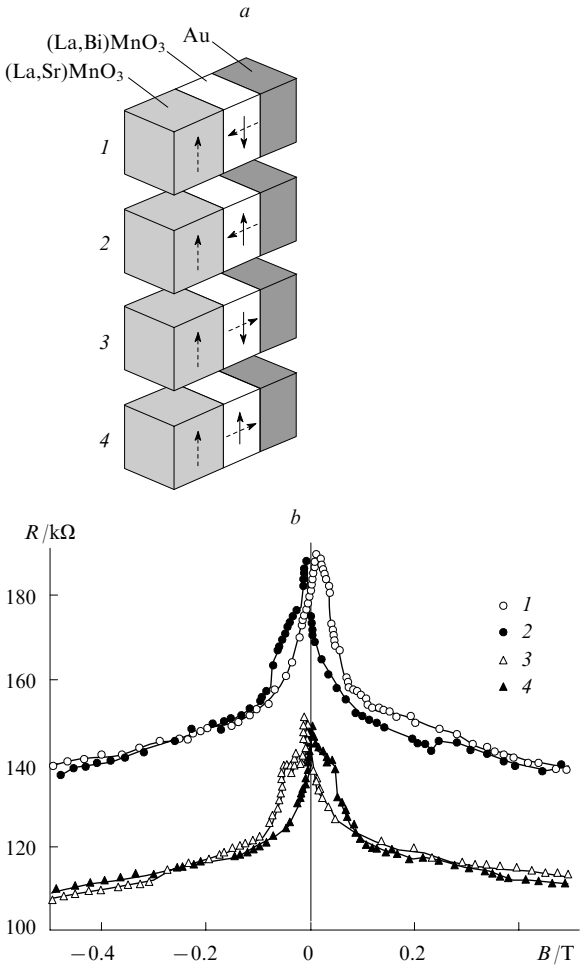


Figure 15. Scheme of a device based on a LSMO/LBMO/Au junction (*a*) and the magnetic field dependences of its electrical resistance ($T = 4$ K) at antiparallel (*1*, *3*) and parallel (*2*, *4*) spins of the barrier and analyser and at different orientations of the electric polarisation of the barrier (*b*).[56]

LSMO/LBMO(2 nm)/Au nanostructure at 4 K obtained under the action of external electric potential of +2 V and −2 V. Electrons pass through the upper gold electrode and become spin polarised when passing through the LBMO dielectric barrier. The role of analyser is played by ferromagnetic LSMO, whose electrical resistance can take two values depending on the spin orientation. However, unlike a conventional spintronic material, here we deal with a multiferroid spin barrier and, as a consequence, the electrical resistance additionally becomes dependent on the electric field polarisation (+2 V or −2 V).

IV. Piezoelectrics

Piezoelectrics are materials in which the electric polarisation of the crystal is related to mechanical distortions by a simple relation

$$P = d\sigma,$$

where d is the piezoelectric coefficient and σ is the mechanical strain. With nonzero electric polarisation it is assumed that piezoelectrics are insulators, *e.g.*, non-cubic oxides, ceramics, *etc*. The piezoelectric coefficient d increases by two orders of magnitude on going from conventional quartz piezocrystals to barium titanate and zirconium titanate piezocrystals. Electrically induced mechanical strain causes the sample to elongate or be compressed by Δl ; the relative elongation can be as high as 10^{-2}. Thus, there are two types of phenomena, *viz*., (i) mechanically induced changes in the electric field and (ii) electrically induced mechanical strain and atomic displacements in materials (in this case, an external electric field is assumed). Nanostructured materials have nondistorted crystal lattices and, as a consequence, exhibit no piezoelectric properties.[57] These phenomena are mainly characteristic of three-dimensional nanomaterials.[58]

Now we will consider the properties of some nanopiezoelectrics, namely, nanowires and nanoplates; mechanical distortions induce a high electric polarisation and e.m.f. in these systems.

1. Nanopiezoelectrics

Piezoelectrics include insulators and semiconductors with high electric polarisation. The most abundant are oxide and chalcogenide nanomaterials in the form of nanowires and nanobelts.[59] Nanowires are used in optics, opto-electronics and piezo-electronics.

Among the semiconductor oxides, ZnO occupes a special position. This unique material is used in optics and electronics as a piezoelectric or a material for piezomechanical devices. In should also be emphasised that ZnO is a biocompatible and biodegradable material; this is important for biological applications.[60]

The piezoelectric properties of ZnO, which are manifested by mechanically distorted samples, will be considered taking ZnO nanowires as an example. The ZnO nanowires were grown on solid or polymeric substrates using Au or Sn as catalysts.[61,62] This made it possible to fabricate hexagonally packed, vertically aligned arrays of ZnO nanowires.

The piezoelectric properties of ZnO nanowires are studied by AFM. Most studies are concerned with the (i) onset of electric polarisation, which is accompanied by generation of the e.m.f. and electric current, and (ii) control of electric current thus generated. ZnO nanowires are suitable for fabrication of wireless nanodevices including current generators, diodes and field-emitting transistors. These devices can be used *in situ* for real-time, self-powered biomedical monitoring. For instance, the biological system can be the source of various kinds of local energy, that is, mechanical, vibrational, chemical and hydraulic energy; conversion of the local energy to electric energy is a topical problem.[63,64]

AFM studies of piezoeffects were carried out using cantilevers with platinum-coated silicon tips.[58] The cantilever contacted the ZnO nanowire under the action of a constant force of ~5 nN. The tip of the cantilever scanned the substrate surface up to the upper end of nanowires, the cantilever being resistance-grounded. Scanning was accompanied by generation of negative voltage peaks (to −6.5 mV) on the substrate. The principles of electricity generation using nanowires can be understood by considering Fig. 16. The phenomenon is based on coupling between the piezoelectric and semiconductor properties of the nanomaterial.[65]

The piezoelectric effect leads to the appearance of an electric potential after elastic deformation of the nanowire, the semiconductor properties are necessary for charge separation and subsequent removal of electric voltage through the rectifying barrier at the metal–semiconductor interface (Schottky barrier). Owing to unique conductivity of ZnO the electric current is high enough for observation. Bending the vertical ZnO nanowire (Fig. 16*a*) by the tip of the cantilever of an atomic force microscope creates a mechanical strain field, namely, the outer surface is stretched (positive strain δ) while the inner surface is compressed (negative strain $-\delta$) (Fig. 16*b*) The electric field E_z acting along the nanowire (along the z-axis) is created due to the piezoelectric effect and its magnitude is given by

$$E_z = \frac{\delta_z}{d},$$

where d is the piezoelectric coefficient along the z-axis, which usually coincides with the c-axis of the ZnO crystal lattice. The piezoelectric field is parallel to the z-axis on the outer surface of the wire and antiparallel to this axis on the inner surface (Fig. 16*c*). At the upper end of the nanowire the electric potential changes from V_s^- (negative) on the compressed surface to V_s^+ (positive) on the stretched surface (Fig. 16*d*). The electric potential[65]

$$V_s^{\pm} = \pm\frac{3ty_{\max}}{4ld}$$

depends on the ratio of the nanowire thickness (t) to its length l (Fig. 16*a*) and on the maximum deviation of the nanowire ($y_{\max}$).

The changes in strain, electric fields and electric potentials (Fig. 16*b*–*d*) were obtained by computer simulation.[58] It should be noted that both voltages (V_s^+ and V_s^-) are due to the piezoelectric effect. Electric potential is due to the displacement of the Zn^{2+} cation relative to O^{2-} anions upon the action of mechanical forces on the structure. Charges cannot move freely or recombine under strain. The potential difference will be non-zero under strain until no additional charges come from the metal.

The discharging process is illustrated in Fig. 16*e*,*f*. The conducting tip of a cantilever, which causes the ZnO nanowire to bend, initially contacts the surface of the stretched

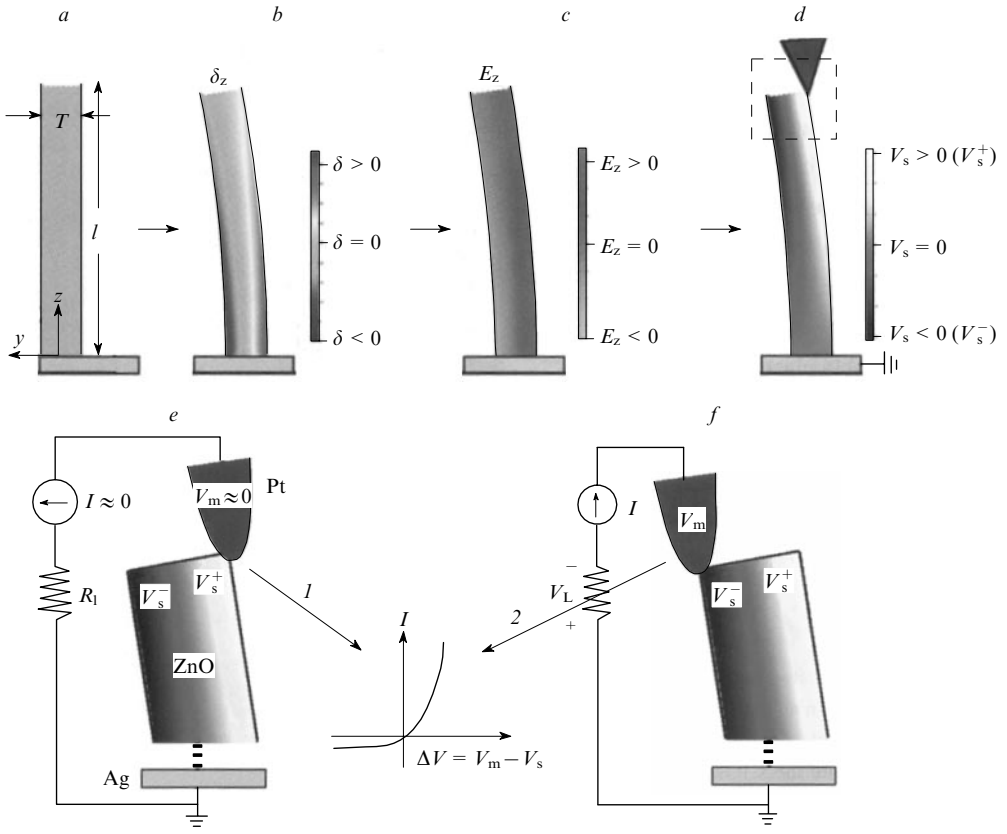


Figure 16. Electricity generation in a ZnO nanowire (*a*), the longitudinal strain δ_z and the strain field distribution after pushing the nanowire by a tip of the cantilever of an atomic force microscope (*b*), the corresponding distribution of the longitudinal electric field E_z, which shows the piezoelectric effect (*c*) and the electric potential distribution in the nanowire (*d*) (dashed line frames the regions shown in Fig. 16 *e* and *f*). The plot represents the current-*vs*.-voltage curve of a diode formed by the Schottky barrier at the metal/conductor interface at inverse (*e*) and direct (*f*) electric current.

part of the nanowire with the potential V_s^+ (Fig. 16 *e*.). The platinum tip of the cantilever has the potential $V_m = 0$; then one has

$$V = V_m - V_s^+ < 0.$$

Since the ZnO nanowires are n-type semiconductors, a Schottky barrier appears at the Pt (metal)– ZnO (semiconductor) junction. In this case, the system represents a reverse-biased Schottky diode and transmits a low current. When the tip of the cantilever interacts with the compressed surface of the nanowire (Fig. 16 *f*), the Pt–ZnO junction is positively charged because

$$\Delta V = V_m - V_s^- > 0,$$

and acts as a forward-biased Schottky diode, namely, the electric current dramatically increases owing to the motion of electrons from the semiconductor nanotube to the metallic tip of the cantilever.

Coupling of piezoelectric and semiconducting properties underlies a new field called nanopiezotronics.[58] This nanotechnology is suitable for converting mechanical energy (*e.g.*, body movement, muscle stretching), vibrational energy (acoustic or ultrasonic waves), hydraulic energy [*e.g.*, a fluid (in particular, blood) flow; blood vessel contraction, *etc*.] to electric energy to power nanodevices. Nanopiezotronics can also find application in wireless devices whose operation is based on conversion of environmental energy. More powerful generators can be fabricated using ZnO nanowire arrays on various metallic, plastic and ceramic substrates.

2. Devices based on piezoelectrics

a. Piezoelectrically controlled diode

The piezoelectric effect observed upon mechanically bending a ZnO nanowire makes it possible to fabricate a gated diode. Using two manipulators, one can study the electrotransport properties of a single nanowire. One tip of a manipulator permanently contacts the nanowire and the other tip is used for bending the nanowire. At the very first moment of contact between the tip of the manipulator and the nanowire, an *I*-*vs*.-*V* curve typical of a conductor is observed. Bending the nanotube at negative voltages causes the electric current to decrease and an asymmetric *I*-*vs*.-*V* curve of a diode is observed. As the bending strain increases, the reverse electric current decreases. Owing to sufficiently high elasticity of the ZnO nanowires all these effects are reversible.

b. Piezoelectric field-effect transistor

A field-effect transistor based on, *e.g.*, carbon nanowires or nanotubes has been quite well studied. The device includes a semiconductor nanowire placed on a silicon substrate covered with a thin oxide layer. The ends of the nanowire are connected to two metallic electrodes. The silicon substrate is

used as the gate electrode. One electrode at the end of the nanowire is the output electrode. The output signal is controlled by the gate voltage.

In the case of a field-effect transistor based on a ZnO nanowire connecting two electrodes, electric current flowing in the nanowire is controlled by the bending strain at the gate electrode, which appears due to the piezoeffect. The piezoelectric field-effect transistor can be considered as a device controlled by weak mechanical forces (to 1 nN). Metallic (tungsten) electrodes have ohmic contacts with the ZnO nanowire. The force bending the ZnO nanowire is exerted to the upper electrode using a piezomechanical actuator. Compression is accompanied by the e.m.f. generation in the nanowire. The *I-vs.-V* curves are symmetrical with respect to zero, which indicates good ohmic contacts between both ends of the ZnO nanowire and the tungsten electrodes.

Further bending of the nanowire causes a great decrease in the electric current. This can be explained by the coupling of the semiconductor and piezoelectric properties of ZnO. The nanowire bears a positive charge on the outer (stretched) surface and a negative charge on the inner (compressed) surface. Charges are induced owing to the piezoelectric effect and ion displacements in ZnO. The electric field distribution suggests two possible mechanisms for the decrease in the electric current, namely, trapping of current carriers and formation of a neutral band. The induction and distribution of the piezopotential over the nanowire can be followed by trapping of electrons (n-type carriers) on the positively charged outer surface; as a consequence, the density of charge carriers will decrease. The opposite (compressed) surface of the nanowire is negatively charged, and when free electrons repel from the charged surface, a neutral band is formed near this surface. Therefore, as the bending of the nanowire increases, the width of the conductivity channel in ZnO decreases and reaches its minimal value when the neutral band reaches the nanowire axis. The maximum bending of the nanowire corresponds to the minimal current. This makes it possible to design a sensor with ultrahigh sensitivity to weak forces.

3. The reverse piezoeffect. Piezoelectric resonator

Piezoelectrics are used in current–motion converters. In particular, acoustic resonators for bulk piezoelectrics are known. These devices are used for fine frequency control in, *e.g.*, navigation systems, space communication systems, *etc.* Usually, they are comprised of a thin piezoelectric plate placed between two electrodes. A radiofrequency signal applied to the plate induces mechanical oscillations, which are in-phase when the plate thickness equals half the wavelength of the output signal. The impedance of the device is minimal at the resonance frequency and maximum under antiresonance conditions. These devices can be used as electronic filters in low-power electronic networks provided miniaturisation to a nano level. Application of piezoelectric resonators as mass sensors for detection of changes in mass upon, *e.g.*, gas adsorption seems to be quite promising. Piezoelectric resonators are fabricated from nanostructured ZnO (so-called ZnO nanobelts).[66, 67]

ZnO nanobelts were grown in a tube furnace over a period of $\sim$12 h to reach the necessary dimensions, *viz.*, the width from 5 to 30 μm and the thickness from a few hundreds of nanometres to 5 μm. The nanobelt could be up to 1 cm long. Nanobelts with these dimensions can be used in modern RF-devices.

ZnO piezoelectric nanobelts are efficient piezoelectric resonators, because they have a highly uniform and defect-free structure. Figure 17 *a* presents a schematic of a nanoresonator based on ZnO. The resonance frequency can be determined by measuring the impedance of the nanobelt when passing an a.c. signal in the case of both signal amplitude and phase measurements. The first and third harmonics (247 and 754 MHz, respectively; Fig. 17 *b*) were determined using two-dimensional vector analysis. Despite broad resonance lines, which characterise a low Q-factor of the device, the third harmonic indicates that the nanobelt operates as resonator.

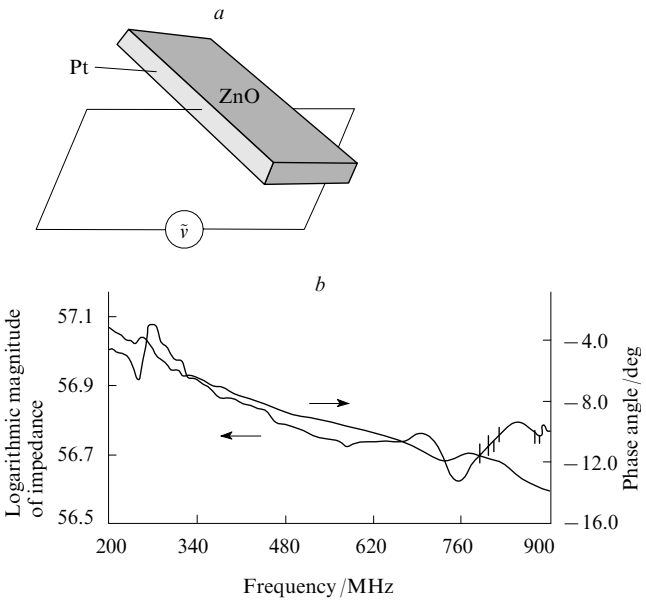


Figure 17. Schematic of a piezoelectric resonator based on ZnO nanobelt (*a*) and the logarithmic magnitude and the phase angle of impedance plotted *vs.* the a.c. frequency (*b*).[67]

Computer simulation allows one to predict the resonance frequency at a specified thickness, density, speed of sound, dielectric constant and some parameters of the device.[68]

In a continuation and elaboration of this research it is natural to assume the design of resonators with progressively decreasing nanobelt thickness. This should lead to an increase in resonance frequency. The resonance frequency can be determined from the assumption that it is inversely proportional to the nanobelt thickness.[68] With a decrease in the nanobelt thickness to the nanometre range the resonance frequencies can increase to the GHz range.

V. Magnetostrictors

Magnetostrictors are materials characterised by coupling between the magnetic ordering and magnetisation and the mechanical strain and lattice distortions. Magnetostriction can be due to both the magnetic dipole or spin–orbit and electronic exchange interactions. The magnetostriction constant

$$\lambda = \frac{\Delta l}{l}$$

can vary from 10^{-5} to 10^{-1}. Metals and alloys with ferromagnetic ordering and high magnetic anisotropy are characterised by the highest magnetostriction constants. Depending on the nature of a material and the magnitude of magnetic field, the magnetostriction constant can be either positive or negative (elongation and compression of the material, respectively).[69]

1. Magnetostrictors and actuators

Magnetostrictive materials are characterised by reversible changes in the magnetically induced deformations and strain as well as by the reverse effects, *i.e.*, the influence of changes in the volume and strain on the magnetic properties.

Now we will consider changes in the length of rods and plates made of various materials ($10^{-4} < \lambda < 10^{-1}$) in external magnetic fields $(0.1-6)\times 10^{-4}$ T. Ferromagnetic materials, which change their volume in weak magnetic fields, can be used for fabrication of acoustic sensors, production of electric motors, actuators, damping devices, speakers and microphones.

Nickel-based magnetostrictive alloys are characterised by the magnetostriction coefficients of up to 5×10^{-5}. The use of rare-earth elements, such as Dy and Tb, enabled significant improvement of magnetostriction, but this is only possible at very low temperatures and the (undesired) hysteresis is large.[70, 71]

The magnetostriction coefficients of binary alloys Tb_xDy_{1-x} are of the order of 10^{-3}; however, low temperatures of magnetic ordering limit the use of these systems to cryogenic temperatures only.[72]

High near-room temperature magnetostriction coefficients were observed for intermetallic alloys $LnFe_2$ (Ln is the rare-earth element), *e.g.*, well-known Terphenol cubic alloys $(Dy_xTb_{1-x})Fe_2$ having high Curie temperatures and high magnetostriction coefficients ($\sim 10^{-3}$).

Not only the high operating temperature and high λ value, but also the saturation magnetostriction in the weakest magnetic fields is very important. Amorphous alloys and metallic glasses, *e.g.*, $Fe_{81}B_{13.5}Si_{3.5}C_2$, are characterised by low saturation magnetostriction ($\lambda = 3\times 10^{-5}$). Despite this fact these materials are suitable for fabrication of sensors owing to the possibility of operation in weak magnetic fields. Preparation of alloys in the systems Fe–Al, Fe–Be and Fe–Ga gave an impetus to progress in this field.[73, 74]

The alloy Fe–15 at.% Al is characterised by $\lambda = 14\times 10^{-5}$ and the alloy Fe–6.8 at.% Be has $\lambda = 10.1\times 10^{-5}$ at room temperature. Non-magnetic atoms Al, Be and Ga increase the interatomic distances and weaken the magnetic interaction between iron atoms, which causes the iron magnetostriction to increase. One can expect an increase in magnetostriction with the increase in the concentration of non-magnetic atoms. Indeed, studies of Fe–Ga alloys showed[74] that the magnetostriction coefficients of single-phase alloys Fe–x at.% Ga (x = 15, 20 and 27.5) with distorted body-centred crystal increase as the concentration of Ga increases. Magnetostriction measurements were carried out using cylindrical rods made of the alloys under study, which were pre-deformed under pressures of up to 50 MPa. Samples were prepared by direct annealing of the entire rod or by annealing in the course of the growth of the rod. The maximum room-temperature magnetostriction coefficients ($27.1\pm 0.2\times 10^{-5}$) in weak magnetic fields ($B < 10^{-2}$ T) were found for the alloy Fe–27.5 at.% Ga obtained by the second technique.

As the gallium concentration increases, the magnetostriction increases while the saturation magnetisation decreases. Thus, indeed the incorporation of gallium into the crystal lattice of iron causes the iron–iron interatomic distance to increase and the magnetisation to decrease. This favours an increase in magnetostriction, which reaches a value of 27.1×10^{-5} in a magnetic field of 65×10^{-4} T.

Yet another way of increasing the magnetostriction is to use intermetallic alloys $LnFe_2$. Compound $Tb_{0.3}Dy_{0.7}Fe_{1.9}$ belonging to this type of alloys has been intensively studied in connection with high room-temperature magnetostriction (to $\sim 200\times 10^{-5}$) in moderate magnetic fields; the change in magnetostriction showed a burst behaviour as function of the applied magnetic field.[75, 76] Figure 18 presents the magnetic field dependences of conventional (smooth) and burst magnetostriction. The sample with burst magnetostriction was pre-treated to create a high magnetic anisotropy. To this end, in addition to specific heat treatment and annealing, the sample was placed in a magnetic field of ~ 1 T.[75] In the case of burst magnetostriction, the parameters $d\lambda/dH$, λ and magnetic hysteresis increase at moderate magnetic fields.

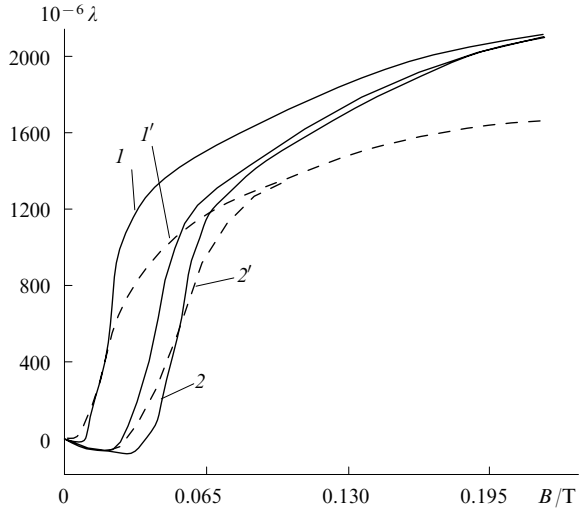


Figure 18. Magnetic field dependences of the conventional (dashed lines) and burst (solid lines) magnetostriction of a $Tb_{0.3}Dy_{0.7}Fe_{1.9}$ single crystal at 7 (*1*, 2) and 14 MPa (*1′*, *2′*).[76]

A model for burst magnetostriction was developed; this allowed one to reveal specific features of the effect. It is assumed that the large derivative $d\lambda/dH$ is due to rotation of the magnetic field components along the directions crossing the magnetoelastic local minimum.

Thus, the burst magnetostriction can be due to a large magneto-crystallographic anisotropy and a narrow distribution of the magnetisation in the crystal. This makes it possible to minimise the interval of magnetic field values corresponding to rotation of the magnetic moments.

Further increase in the magnetostriction coefficient enables fabrication of magnetostrictive devices, in which the action of a permanent or alternating magnetic field leads to large atomic displacements or changes in vibrational amplitudes. For instance, the crystal Ni–Mn–Ga is char-

acterised by $\lambda = 6\%$ in permanent and $\lambda = 3\%$ in alternating magnetic field.

Magnetically induced static and dynamic deformations were observed for a (100)-oriented $Ni_{49.7}Mn_{29.0}Ga_{21.3}$ single crystal.[77] This alloy belongs to so-called 'shape memory alloys' capable of undergoing martensite transformations depending on the temperature and shape of the sample. Single crystals made it possible to develop tensile deformations induced by transverse magnetic field (Fig. 19). As a consequence, the single crystal forms a twin structure with the shear-induced twin boundaries. A static shear deformation of 6% was induced by a constant magnetic field of 0.6 T. Dynamic strain in a 2-Hz alternating magnetic field was 2.6%, the saturation magnetostriction being attained in the range 0.4–0.5 T. Shear deformation of the sample causes an increase in the saturation magnetostriction at a pressure of 1.9 MPa and a subsequent decrease in it. If the pressure is lower than the optimal pressure, the strain is not relieved as the magnetic field returns to zero and the elongation of the sample is retained. If the strain is higher than the optimal value, the magnetic field is too weak to relieve the strain and thus one gets a zero elongation of the sample. The $d\lambda/dB$ maximum is twice as high as that of the magnetostrictive material Terfenol (see above).

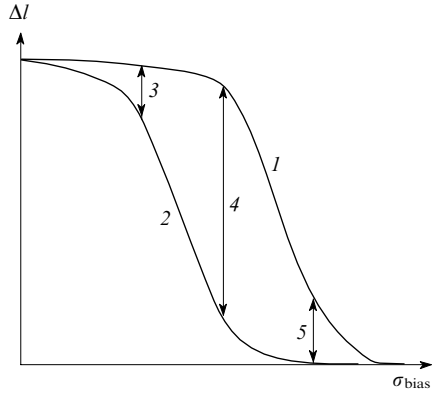


Figure 19. Phase diagram of magnetic field induced transformation of an actuator along the normal to the direction of lateral deformation (shown by arrows).
Also shown are the regions of strain-induced twinning of the single crystal.
Magnetic field induced tension (*1*), compression (*2*), shear deformation (*3*, *5*) and the limiting dynamic deformations (*4*).

2. Magnetostrictive oxide nanomaterials

The most pronounced manifestations of the magnetic properties of materials are related to the magnetic phase transitions in iron oxide nanoclusters and nanostructures. Magnetic phase transitions are of interest for both basic research and practical applications. In most bulk magnetics, second-order phase transitions occur, but the first-order phase transitions also occur in some compounds. They are accompaned by changes in the volume both on giong from the magnetically ordered state to the paramagnetic state and upon change in the type of magnetic ordering. These compounds include, *e.g.*, MnAs (ferromagnetic → paramagnetic), MnO, UO_2, Eu (antiferromagnetic → paramagnetic), α-Fe_2O_3 (antiferromagnetic → weak ferromagnetic).[69, 78]

Magnetic phase transitions are of particular value for nanoclusters and nanostructures, because new factors (compared to bulk materials) manifest themselves in these systems. These are the size effects, surface effects, cluster–cluster interactions, interactions between nanoclusters and the matrix, *etc.*; they change the character and mechanism of the phase transitions. In addition, the surface tension for 1–10-nm nanoclusters corresponds to pressures of a few GPa, which is much higher than the pressures required for the observation and control of magnetostriction (tens of MPa).

Specific features of magnetic transitions can be used as a new tool for exploring the structure of nanosystems and for the design of novel nanomaterials and nanodevices.

Nanoclusters and nanomaterials undergo both the first- and second-order magnetic phase transitions. The second-order magnetic phase transitions in the metal and metal oxide clusters, as well as in most bulk magnetics, are characterised by the Langevin dependences of the magnetisation, a gradual decrease in magnetic ordering and spontaneous magnetisation near the Curie or Néel temperatures. In addition, nanoclusters smaller than 10 nm in size exhibit superparamagnetic properties, which leads to efficient decrease in the Curie and Néel temperatures.

Some nanostructured metal oxides (nanoclusters) exhibited the first-order magnetic phase transitions accompanied by jumpwise loss of spontaneous magnetisation at a certain temperature or upon a decrease in the cluster size down to certain critical value and experienced a transition to the paramagnetic rather than superparamagnetic state.[79–81]

First-order magnetic phase transitions of isolated clusters (clusters with weak cluster–cluster interactions) and of the nanostructures comprised of clusters smaller than 100 nm (characterised by strong cluster–cluster interactions) manifest themselves in different fashion. The reasons for and mechanisms of magnetic phase transitions are different; therefore, it is appropriate to consider separately the first-order magnetic phase transitions of the nanosystems comprised of isolated nanoclusters smaller than 10 nm in size and those of the nanostructures built of larger (particle size to 100 nm) strongly interacting clusters.

a. Nanosystems with isolated clusters

The magnetic ordering of a cluster is a co-operative phenomenon; *i.e.*, there should exist a critical cluster size corresponding to the loss of magnetic ordering and magnetisation. This parameter was determined using the thermodynamic model for magnetic phase transitions.[80] The model also predicts the first-order magnetic phase transitions in nanoclusters and changes in the character of transition depending on the cluster size.

Yet another model[80] relates the Curie (Néel) temperature to the change in volume

$$T_C = T_0\left(1 + \beta\frac{V - V_0}{V_0}\right), \qquad (3)$$

where T_0 is the Curie temperature of the uncompressed compound;

$$\beta = \frac{\partial(T_C - T_0)}{\partial(V - V_0)};$$

V and V_0 is the molar volumes of the compound in the magnetically ordered (compressed) and nonmagnetic (para-

magnetic) states, respectively. It is commonly accepted that this dependence of the critical transition temperatures on the volume is required for the first-order magnetic transitions in nanoclusters to occur.

The change in the Gibbs free energy of a cluster on going from the magnetically ordered to the non-magnetic state is described by the relation, which accounts for the changes in the cluster volume caused by pressure-induced magnetostriction (compressibility). The pressure is given by

$$p = \frac{2\alpha}{R}$$

and is due to the surface tension (α) of the cluster radius R,

$$\Delta G = -\frac{1}{2}NkTm^2 + \frac{1}{2\eta}\left(\frac{V - V_0}{V_0}\right)^2 + \frac{2\alpha}{R}\frac{V - V_0}{V_0} + \tag{4}$$

$$+ \frac{1}{2}NkT\left[\left(\ln\frac{1-m^2}{4}\right) + m\ln\frac{1+m}{1-m}\right].$$

Here N is the number of atoms having a spin of 1/2, k is the Boltzmann constant, $m = M/M_s$ is the relative magnetisation and η is the volume compressibility. This equation includes four terms. The first term describes the exchange energy density; the second term is the cluster deformation energy; the third term is the surface energy; and the fourth term is the entropy contribution, which ensures the Langevin-type temperature dependence of the magnetisation.

A stable magnetic state of a cluster requires that the free energy, as function of the changes in the cluster volume and magnetisation upon the magnetic phase transition, be minimal. Solving the system of equations

$$\frac{\partial\Delta G}{\partial V} = 0, \tag{5}$$

$$\frac{\partial\Delta G}{\partial m} = 0,$$

which define the equilibrium state of the system, gives

$$\frac{T}{T_{C0}} = \left(m\frac{1}{3}\gamma m^2 + 1\right)\left(\frac{1}{2}\ln\frac{1+m}{1-m}\right)^{-1}, \tag{6}$$

where

$$\gamma = \frac{3}{2}\frac{NkT_0\eta\beta^2}{1-\eta\beta p},$$

and the Curie temperature

$$T_{C0} = T_0(1-\eta p)$$

is lower than T_0 due to the development of the pressure induced by the surface tension of the cluster.

Figure 20 presents the calculated temperature dependences of the relative magnetisation at different values of the parameter γ, which specifies the character of the magnetic phase transition. In particular, the range $\gamma < 1$ corresponds to the second-order magnetic phase transitions, whereas the range $\gamma \geqslant 1$ corresponds to the first-order magnetic phase transitions. This portion of the curve corresponds to an increase in the free energy, *i.e.*, to unstable magnetic

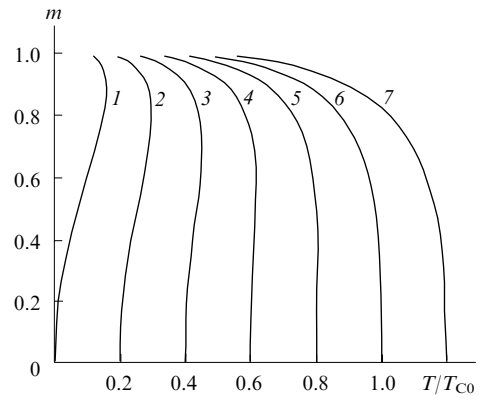


Figure 20. The relative magnetisation of a cluster plotted *vs.* temperature at different γ values
The dashed line describes the jump-like change in the magnetisation, which corresponds to a first-order magnetic phase transition.
$\gamma < 1$ (*1*), $\gamma = 1$ (*2*) and $\gamma > 1$ (*3*).

structures. Knowing the γ value, one can estimate the critical cluster size corresponding to the jumpwise transition from the magnetically ordered to paramagnetic state. For the sake of convenience, the parameter γ can be represented as follows:

$$\gamma = \frac{T_{Cc}}{T_{C0}}, \tag{7}$$

where T_{Cc} is the Curie temperature of the cluster

$$T_{Cc} = \frac{3}{2}NkT_0^2\eta\beta^2.$$

If $\gamma \geqslant 1$ and

$$R \leqslant R_{cr} = \frac{2\alpha\beta\eta}{1 - T_{Cc}/T_0}, \tag{8}$$

a first-order magnetic phase transition occurs and clusters undergo a transition to the paramagnetic state.

Large clusters ($R > R_{cr}$) lose their magnetisation due to the second-order magnetic phase transitions as the temperature increases.

For the first-order magnetic phase transitions to occur, the compressibility of clusters should be high enough. (Zero-compressibility clusters correspond to second-order magnetic phase transitions.) The key parameter responsible for the manifestation (or lack) of the first-order magnetic phase transitions and variation of the critical cluster size [see Eqns (5)–(8)] is the surface tension. This model for phase transitions considers an isolated cluster characterised by the surface tension α at the cluster/vacuum interface. Any interaction of the cluster with the cluster-stabilising matrix and with the neighbouring clusters leads to a decrease in α and R_{cr} and the first-order magnetic phase transitions will no longer occur. Thus, investigations of the first-order magnetic phase transitions can serve a tool for characterisation of cluster–cluster and cluster/interface interactions.

To observe the first-order magnetic phase transitions of nanoclusters, a nanosystem comprised of iron ferrihydrite nanoclusters in Polysorb pores 13 to 75 nm in diameter was

synthesised.[80] This matrix nanosystem makes it possible to prepare individual metal oxide clusters or to accumulate a number of clusters in a single pore. Polysorbs are styrene/divinylbenzene copolymers. Due to the lack of functional groups grafted on the surface the Polysorb pore walls exhibit hydrophobic properties; as a consequence, the interaction between $Fe_5HO_8 \cdot 4H_2O$ (ferrihydrite) clusters and the matrix weakens and the critical cluster size R_{cr} increases. The cluster–cluster interactions and the number of clusters in pores were changed by varying the concentration of iron atoms in the Polysorb pores. To ensure the use of Mössbauer spectroscopy (the method is highly efficient in studies of such systems) and to improve the sensitivity of the technique, experiments were carried out with ^{57}Fe-enriched, iron-containing clusters, which were sysnthesised in pores by impregnating Polysorbs with an alcohol solution of $^{57}FeCl_3 \cdot 6H_2O$ (concentrations were $c = 1.2 \times 10^{-2}$ and 1.2×10^{-3} mol litre^{-1}) followed by blowing air containing gaseous ammonia impurity. An increase in the pore size from 13 to 75 nm caused the size of the clusters in the Polysorb pores to increase.

Figure 21 presents the Mössbauer spectra of ferrihydrite clusters in Polysorb pores at the concentration $c = 1.2 \times 10^{-3}$ mol litre^{-1} at different temperatures. At all temperatures, the spectra exhibit a magnetic HFS with narrow lines and a paramagnetic central doublet. An increase in temperature is accompanied by partial transformation of the HFS to the paramagnetic doublet bypassing the spectra corresponding to the superparamagnetic line broadening accompanied by a considerable decrease in the magnetic field at the nucleus. With allowance for these results one can suggest the occurrence of the first-order magnetic phase transitions in the ferrihydrite clusters in the temperature range $4.2 < T < 10$ K under these conditions.

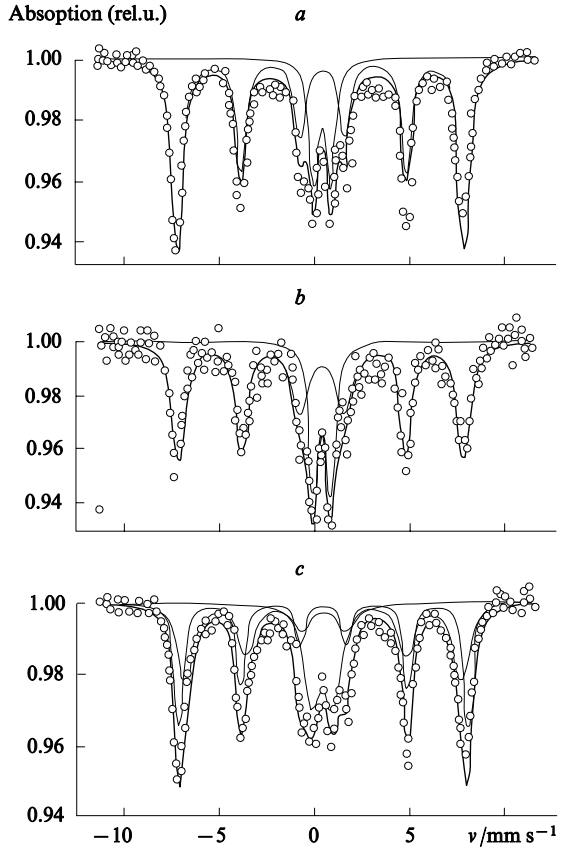


Figure 21. Mössbauer spectra of ferrihydrite clusters in Polysorb with a pore size of 13 (*a*, *b*) and 20 nm (*c*); Fe concentration $c = 1.2 \times 10^{-3}$ mol litre^{-1}.
$T = 4.2$ K (*a*, *c*) and 10 K (*b*).

By analysing the Mössbauer spectra[80] one can determine how the cluster–pore wall interaction and cluster–cluster interactions affect the character of the magnetic phase transitions. The concentration $c = 1.2 \times 10^{-3}$ mol litre^{-1} corresponds to almost a single ferrihydrite cluster of size 1–2 nm in a pore of volume 10^{-22}–10^{-23} m^3; the magnetic properties of the cluster will depend on the character of its interaction with the matrix surface.

Thus, the first-order magnetic phase transition is observed at 4.2 K. A proportion of small clusters (cluster size is less than R_{cr}) lose their spontaneous magnetisation in jumpwise manner and go to the paramagnetic state. An increase in the pore size to 20 nm at the same concentration of iron atoms is accompanied by an increase in the cluster size and subsequent increase in the proportion of the magnetic HFS and a decrease in the probability of the first-order magnetic phase transitions. A tenfold increase in the ^{57}Fe concentration at the same pore size is followed by nucleation of more than one cluster in a single pore (to 5–8 clusters of size $\sim$2 nm),[82] strengthening of cluster–cluster interactions and, as a consequence, by the overall decrease in R_{cr} for the first-order magnetic phase transitions. However, now this effect can be used for estimating the size of the ferrihydrite clusters participating in superparamagnetic relaxation. From the relation

$$\tau_s = \tau_0 \exp \frac{KV}{kT} \tag{9}$$

for the clusters with the concentration $c = 1.2 \times 10^{-2}$ mol litre^{-1} at $\tau_0 = 1 \times 10^{-9}$ s, $T = 10$ K and the magnetic anisotropy constant $K = 1.7 \times 10^5$ J m^{-3} one gets $\tau_s \sim 189 \times 10^{-9}$ s; the upper limit of the cluster size was estimated at $\sim$2.2 nm. Thus, both the first-order and second-order (superparamagnetism) magnetic phase transitions were observed in nanosystems for $\sim$2-nm clusters; magnetic phase transitions were observed in the temperature range 4.2–6 K.

It is interesting to compare the experimental estimates of R_{cr} made from the Mössbauer spectra, from the concentration of iron atoms in pores and from the results of calculations using relations (6)–(8). For the critical temperature of the first-order magnetic phase transition $T_{Cc} \approx 4.2$–6 K, the second-order magnetic phase transition temperature (blocking temperature) $T_0 \sim 20$–30 K (for small clusters), the molar volume $V_m = 14.4 \times 10^{-29}$ m^3, $1/\eta \sim 1.5 \times 10^{11}$ Pa, and $\alpha \approx 1$ J m^{-2} one gets $R_{cr} \approx 1$ nm, which agrees with the experimental estimates ($R_{cr} \approx 1.5$–2 nm). Some indications of the first-order magnetic phase transitions were observed in studies of small clusters of other iron oxides (see, *e.g.*, Ref. 81); however, they were not observed for metal clusters (Fe, Co, Ni) presumably due to lower compressibility.

Pressure is an important factor responsible for the occurrence or lack of the first-order magnetic phase transitions. According to the thermodynamic model for magnetic phase transitions in nanoclusters (6)–(8), the critical

transition temperature decreases as the external pressure increases as follows

$$T_{C0} = T_0 (1 - \beta\eta P). \tag{10}$$

As the specific external pressure (pressure per cluster) changes from p_0 by Δp, the magnetic transition temperature of the cluster is changed by

$$\Delta T_{C0} = T_0 \left[1 - \beta\eta \left(p_0 + \Delta p + \frac{2\alpha}{R} \right) \right] - T_{C0}. \tag{11}$$

From here it follows

$$\Delta T_{C0} = -T_0 \beta\eta \Delta P. \tag{12}$$

Then one has

$$\frac{\Delta T_{C0}}{T_{C0}} = \Delta p \left(\frac{2\alpha}{R} + p_0 - \frac{1}{\beta\eta} \right)^{-1}. \tag{13}$$

At $p_0 \ll 2\alpha/R$, one can take that

$$\frac{\Delta T_{C0}}{T_{C0}} = \Delta P \left(\frac{2\alpha}{R} - \frac{1}{\beta\eta} \right)^{-1}. \tag{14}$$

The temperature dependences of the relative magnetisation calculated using relation (6) at different pressures are shown in Fig. 22. As the pressure increases, the phase transition temperature decreases. These calculations also suggest that an increase in pressure should cause the transition probability of the cluster to the non-magnetic state to increase owing to first-order magnetic phase transitions.

Thus, pressure treatment of a cluster nanosystem should lead to a decrease in the Curie (Néel) temperatures. There is a simple procedure for producing an excess pressure in a finite volume by freezing water in it. The volume of ice is 8% larger than that of water and thus one can produce pressures of up to a few GPa in nanopores.

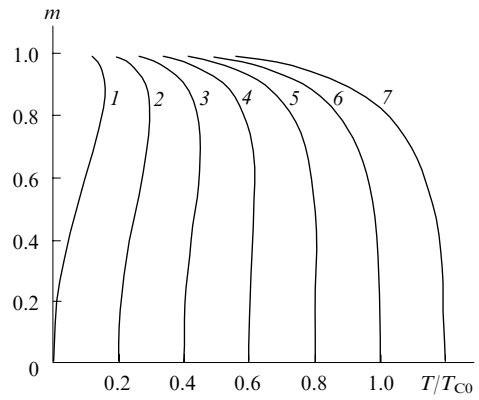


Figure 22. The relative magnetisation of clusters at different pressures plotted *vs.* temperature.[83]
$10^{-9} p$ /Pa: 1.25 (*1*), 1.2 (*2*), 1.15 (*3*), 1.1 (*4*), 1.05 (*5*), 1 (*6*) and 0.95 (*7*).

To study the hydration and freezing of nanostructures and the action of pressure on clusters upon freezing of water in nanopores, two series of experiments with nanocluster systems representing anhydrous and hydrated iron oxyhydroxide clusters in sulfonate cation exchange resin were carried out.

Mössbauer spectroscopy is an efficient method of investigation of magnetic phase transitions in these nanoclusters and in ferrihydrite clusters. Iron oxyhydroxide clusters were prepared in sulfocationite (styrene/divinylbenzene copolymer) pores by ion exchange from ^{57}Fe-enriched aqueous iron chloride followed by precipitation of iron hydroxide clusters upon treatment with NaOH.[83] Clusters thus obtained were $\sim$3 nm in size in both anhydrous and hydrated nanosystems. The spectral processing procedure involved resolution of the quadrupole doublet and magnetic HFS with allowance for the magnetic field distribution. The Mössbauer spectra of the anhydrous and hydrated iron hydroxide clusters are presented in Fig. 23. They mainly differ in the temperature range 8.5–15 K.

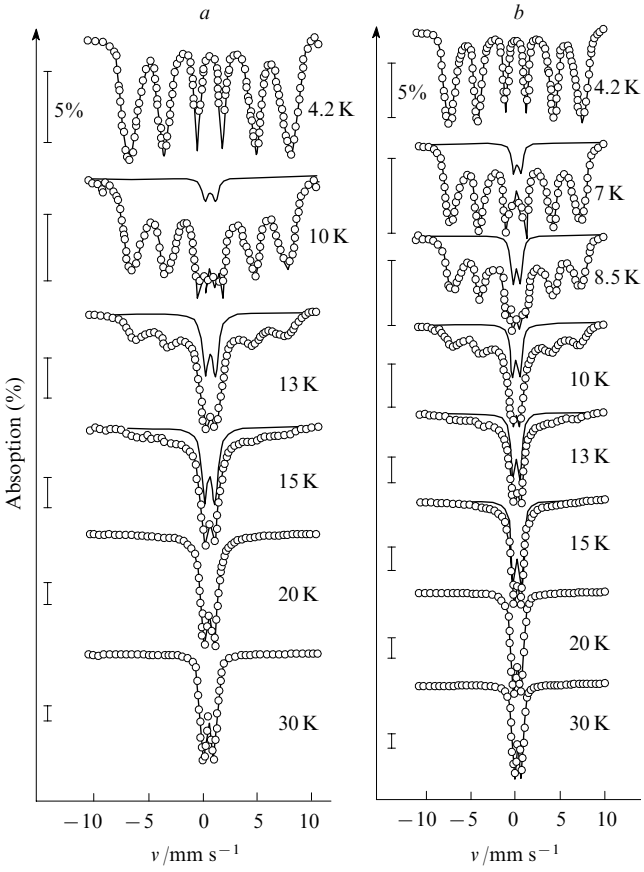


Figure 23. Mössbauer spectra of iron oxyhydroxide clusters in anhydrous (*a*) and hydrated (*b*) sulfonate cation exchange resin at different temperatures.

In particular, freezing of the nanosystem causes the relative intensity of the quadrupole doublet to increase from 7.2% to 17.2% at $T = 10$ K. Changes in the spectra of sulfonate cation exchange resin indicate an increase in the intensity of the central quadrupole doublet in the hydrated state. A comparison shows that the spectra of anhydrous sulfocationite samples containing iron oxyhydroxide clusters at 13 K (Fig. 23 *a*) are identical to those of hydrated samples at 10 K (Fig. 23 *b*); this suggests a shift of the magnetic phase transition temperature upon hydration.

When freezing water, the excess pressure experienced by the cluster is mainly determined by the deformation of the polymer matrix. Deformation-induced strain developed in the matrix is transferred to the cluster either by the matrix or through the ice phase. The excess pressure can be estimated from the relation

$$\Delta p = \frac{1}{\eta_m} \ln \frac{V_2}{V_1}, \tag{15}$$

where η_m is the compressibility of the matrix at the crystallisation temperature of water; and V_1 and V_2 are the unit cell volumes of the matrix before and after crystallisation of water. Since

$$\frac{V_2}{V_1} = \frac{V_1 + \Delta V}{V_1} = 1 + \frac{\Delta V}{V_1},$$

at $\Delta V/V_1 \ll 1$ one can assume that

$$\Delta p = \frac{1}{\eta_m} \frac{\Delta V}{V_1}. \tag{16}$$

At an ice density at 0 °C of 0.917 kg m^{-3} and a water density of 0.999 kg m^{-3} one gets $\Delta V/V_1 \approx 0.09$.

Thus, the excess pressure acting on the cluster in the frozen hydrated organic matrix characterised by $1/\eta_m = (5-10) \times 10^9$ Pa is $\Delta p = (0.45-9) \times 10^9$ Pa. This is comparable with the pressure in the cluster of radius 1.5 nm, developed due to the surface tension. In particular, at $\alpha = 1$ J m^{-2} one has $p_\alpha = 2\alpha/R = 10^9$ Pa. At the same time, consideration of this effect in the framework of the thermodynamic model for magnetic phase transitions with inclusion of the effect of pressure on the cluster [see Eqns (6)–(8)] allows the change in the pressure-induced shear temperature to be estimated. An increase in pressure causes the magnetic phase transition temperature to decrease by

$$\frac{\Delta T_{C0}}{T_{C0}} \approx \frac{1}{\eta_m} \left(\frac{2\alpha}{R} - \frac{1}{\beta\eta} \right)^{-1} \frac{\Delta V}{V}. \tag{17}$$

The ΔT_{C0} value can be estimated using the following parameters: $\alpha \approx 10^9$ Pa, $\beta \approx 10^2$, $\eta \approx 10^{-11}$ m^2 J^{-1} and $1/N \approx 10^{-28}$ m^3. From this one gets

$$\Delta T_{C0} = (0.1-1.0) T_{C0}. \tag{18}$$

By reducing ΔT_{C0} by 1–2 decimal orders one can attain T_{C0}. The interval ΔT_{C0} can be estimated from the Mössbauer spectra (see Fig. 23) in which the intensity of the doublet in the spectra of hydrated samples at a certain temperature equals the intensity of the doublet in the spectra of anhydrous samples, measured at a higher temperature.

The temperature shift thus obtained for the clusters in cationite is $\Delta T_{C0} = 3-4$ K and agrees with the thermodynamic estimates.

It sholuld be noted that the term $\Delta T_{C0}/T_{C0}$ in relation (17) is proportional to $\Delta V/V$. However, the coefficient of proportionality strongly depends on the quantity $(2\alpha/R - 1/\beta\eta)^{-1}$. As a result, we get that for a cluster characterised by a particular size, high compressibility and magnetostriction one can expect a significant increase in this coefficient and thus an appreciable improvement of the sensitivity to excess pressure. In this case, the transition of the cluster from the magnetically ordered to the non-magnetic (paramagnetic) state can be induced by a relatively low pressure ($10^5 - 10^6$ Pa).

b. Nanostructures

First-order magnetic phase transitions induced by cluster–cluster strain and defects also occur in nanosystems containing large nanoclusters (30–50 nm in size). Such nanostructures are formed in solid-phase chemical reactions, *e.g.*, sintering of nanoparticles, and are characterised by strong cluster–cluster interactions. The first-order mag-

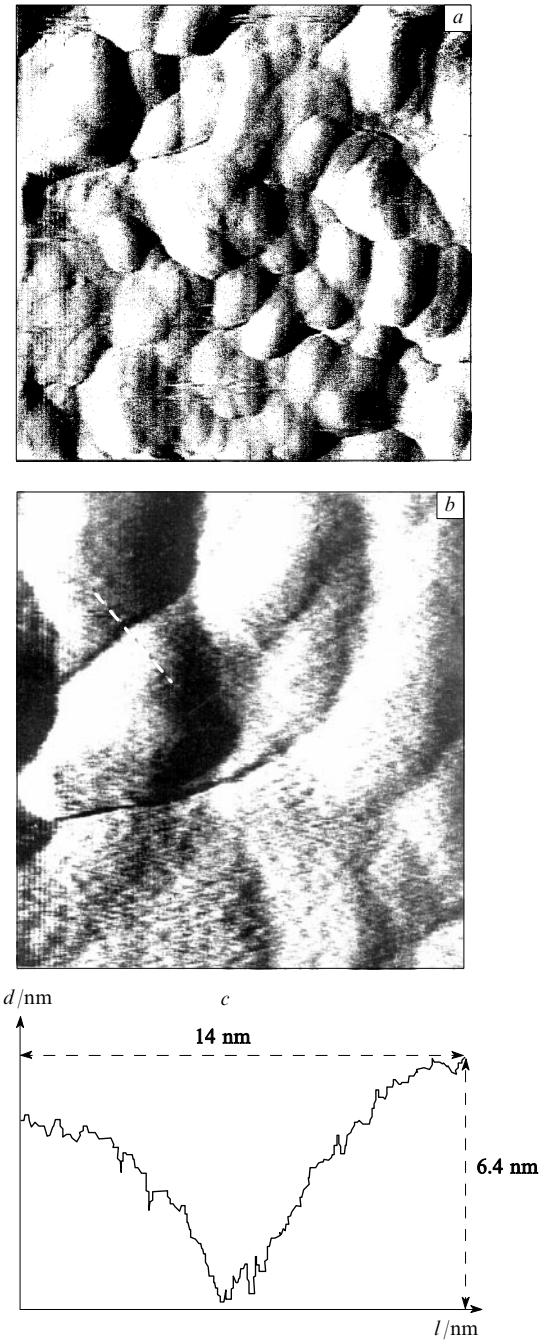


Figure 24. AFM images of a nanocluster system composed of α- and γ-Fe_2O_3 clusters [scale length 500 (*a*) and 150 nm (*b*)] and the surface profile (*c*) along the dashed line shown in the left part of Fig. 24*b*.

netic phase transitions similar to the transitions in the ferrihydrite clusters 1–3 nm in size[80] were observed in a nanostructure formed in the early stage of the sintering of α-Fe_2O_3 and γ-Fe_2O_3 nanoparticles.[84,85] The AFM images of this nanostructure are shown in Fig. 24.

The Mössbauer spectra of the nanostructure comprised of α- and γ-iron oxides at different temperatures are presented in Fig. 25. Raising the temperature is accompanied by magnetic phase transitions from the ordered magnetic state of the nanostructure with the magnetic HFS to the paramagnetic (superparamagnetic) state. At 77 K, the spectra exhibit two systems of magnetic HFS corresponding to α-Fe_2O_3 and γ-Fe_2O_3. As the temperature increases to 120 K, a quadrupole doublet appears in the spectra, but the overall spectral pattern remains unchanged. Starting with 120 K, the spectra undergo transformation and now represent a single system of magnetic HFS (no quadrupole splitting). In the temperature range 120–300 K the Mössbauer spectra show reversible transformation of the magnetic HFS to the paramagnetic doublet without noticeable shift or broadening of spectral lines characteristic of the second-order magnetic phase transitions or superparamagnetism. This is an indication of the first-order magnetic phase transitions (magnetisation of the nanomaterial vanishes in jumpwise fashion). These transitions occur at the critical temperatures (120–300 K) that are lower than the critical temperatures T_0 of the bulk samples of α-Fe_2O_3 and γ-Fe_2O_3 (856 and 965 K, respectively). The lack of superparamagnetism in these large clusters clearly follows from relation (9). Using the magnetic anisotropy constant $K \approx 10^5$ J m^{-3} and $\tau_0 = 10^{-9}$–10^{-10} s, the relaxation time of the magnetic moment (τ) will be a few orders of magnitude longer than the measurement time (period of Larmor precession for ^{57}Fe is about 10^{-8} s). Thus, the superparamagnetism of these nanostructures has no effect on their magnetic properties and cannot lead to a decrease in T_{C0}.

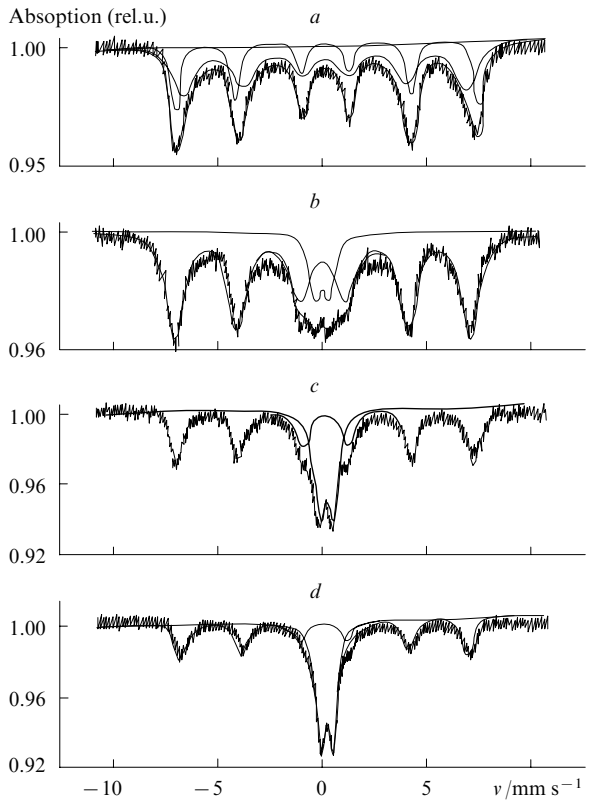


Figure 25. Mössbauer spectra of a nanostructure composed of iron oxide nanoclusters, prepared at the decomposition temperature of iron oxalate (265 °C).
Measured at 77 (*a*), 120 (*b*), 160 (*c*) and 300 K (*d*).

The magnetisation and magnetic ordering of the α-Fe_2O_3/γ-Fe_2O_3 nanostructure vanish due to the first-order magnetic phase transition (magnetic field jumpwise decreases from 50 to 0 T). It should be noted that there exists the critical size ($\sim$1.5 nm) of isolated ferrihydrite clusters; smaller clusters undergo a jumpwise transition to the paramagnetic state.[80] There is also a narrow temperature interval (4.2–10 K) characteristic of the first-order phase transitions. These effects are due to the influence of the surface tension.

For clusters 30–50 nm in size, the surface tension induced pressure should be an order of magnitude lower; in addition, the surface tension decreases if the cluster–cluster interaction is strong. Therefore, there should be some other reasons for magnetic phase transitions in this nanostructure and for the decrease in T_{C0} corresponding to $\gamma \geqslant 1$. Clearly, this can be due to the influence of defects in the nanostructure on its properties.[86] The maximum density of defects is assumed for iron oxide clusters 20–50 nm in size. For larger clusters, the contribution of surface as the source of defects is small, while for small clusters, the surface pressure is high enough to displace defects out of the cluster; thus, these clusters are defect-free.[86]

According to this model, there should exist a maximum density of defects, which is responsible for the critical cluster size equal to a few tens of nanometres. Indeed, a feature of the smaller clusters is the occurrence of the first-order magnetic phase transitions, whereas larger clusters undergo second-order magnetic phase transitions characteristic of bulk materials.

The maximum in the dependences of the defect concentration on the cluster size[86–88] also manifests itself in the temperature dependences of the magnetisation of the structure comprised of different-size clusters. One can assume a linear dependence of the critical temperature on the concentration of defects in the cluster. Then one has

$$T_C = T_{C0}(1 + \beta c_v), \tag{19}$$

where $\beta < 0$, c_v is the concentration of defects.

The thermodynamic potential of the nanosystem 'magnetic clusters–medium–defects' with allowance for magnetic cluster–cluster interaction can be written as the sum including the surface energy of the cluster and the change in the chemical potential due to the change in the cluster size and the density of defects

$$G = \Delta\mu n_v + \alpha s n_v - \frac{1}{2} N_v k T_{C0}(1 + \beta c_v) m^2 + \tag{20}$$

$$+ NkT\left[\left(\frac{1}{2}\ln\frac{1-m^2}{4}\right) + m\ln\frac{1+m}{1-m}\right],$$

where

$$\Delta\mu = \mu_0 + kT\ln\frac{N_s n_v}{N_v n_s}$$

is the chemical potential difference between the defects located in the interior and on the surface of the cluster; n_v

is the number of defects in the cluster; N_v is the number of atoms in the cluster; n_s is the number of defects in the inter-cluster medium per cluster; N_s is the number of atoms in the inter-cluster medium per cluster; α is the surface tension of the cluster; s is the cluster surface area; $m = M/M_0$ is the relative magnetisation of the cluster; and N is the number of spins in the cluster. The energy minimisation conditions

$$\frac{\partial \Delta G}{\partial c} = 0,$$

$$\frac{\partial \Delta G}{\partial m} = 0$$

and the definition of the equilibrium state lead to the theoretical temperature dependence of magnetisation for different cluster sizes,[87] shown in Fig. 26 for iron oxide as an example.

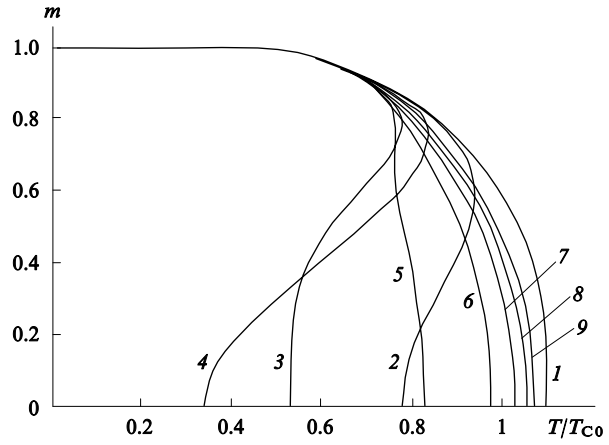


Figure 26. Temperature dependence of the relative magnetisation of iron oxide at R/a = 6 (*1*), 12 (*2*), 25 (*3*), 50 (*4*), 100 (*5*), 200 (*6*), 300 (*7*), 400 (*8*), 500 (*9*).
R is the cluster radius and a is the lattice constant.

The dependence described by Eqn (20) was plotted using the data taken from Ref. 87 and predicts the existence of a critical size of oxide clusters (30 – 40 nm), corresponding to the maximum density of defects. In the larger and in the smaller clusters, the first-order magnetic phase transitions are transformed to second-order magnetic phase transitions.

c. Magnetic phase transitions in nanostructures induced by shear stress under pressure

Using shear stress under high pressure, one can attain nanostructuring of bulk samples and compaction of nanocrystallites to 5 – 10 nm in size. Simultaneously, plastic deformation generates numerous defects, which affect the magnetic properties of nanostructures, in particular, the character and critical parameters of magnetic phase transitions. Consider nanocomposites containing the α-Fe_2O_3 and γ-Fe_2O_3 nanoclusters, which retain the strained state of and defects in the nanosystem upon unloading. In these systems one can observe first-order magnetic phase transitions and a further decrease in T_{C0} due to an increase in the density of defects. For bulk samples nanostructuring should also lead to shift of the critical temperatures and to changes in the character of magnetic phase transitions (first-order to second-order transitions or *vice versa*). Now we will dwell on magnetic phase transitions in two types of nanosystems based on α-Fe_2O_3 and γ-Fe_2O_3 nanoclusters of size 20 – 50 nm (**1**) and on metallic europium (**2**). Nanosystem **1** contained α-Fe_2O_3 and γ-Fe_2O_3 nanoclusters of size 20 – 50 nm (**1a**) and 30 – 50 nm (**1b**; here, 50% of monomeric acrylamide was also added). Nanosystem **2** contained metallic europium (**2a**), metallic europium and the α-Fe_2O_3 and γ-Fe_2O_3 nanoclusters of size 30 – 50 nm (1%; **2b**) and metallic europium with adamantane (10%; **2c**).[87, 88]

A high-pressure setup equipped with Bridgeman anvils allowed one to develop a pressure of up to 5 GPa with simultaneous accumulation of shear with an increment of 10° per 5 s. The pressure developed in the experiments reached a value of 2 GPa and the turn angle of the anvils was varied from 120 to 240°.

Shear stress under pressure (to 2 GPa) causes polymerisation of acrylamide. When unloaded, the polymer retained the shear deformation of the sample containing nanoclusters α-Fe_2O_3 and γ-Fe_2O_3, thus precluding their recrystallisation and recovery of the previous phase equilibrium. Joint action of shear stress and pressure led to an increase in the proportion of the non-magnetic component in system **1b**. An unusual result was obtained for nanosystem **2b**.

The ^{57}Fe Mössbauer spectrum of nanostructure **2b** exposed to shear stress under pressure (T = 300 K, Fig. 27) exhibits an almost complete loss of magnetic ordering in the α-Fe_2O_3 and γ-Fe_2O_3 clusters, which indicates a decrease in the average size of nanocrystallites and a decrease in the Curie (Néel) temperatures below room temperature.

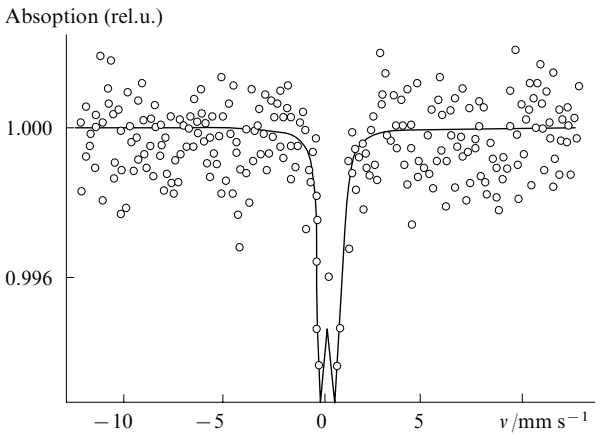


Figure 27. Room-temperature ^{57}Fe Mössbauer spectrum of the nanostructure 2.2 after pressure treatment at 2 GPa; the turn angle of anvils was 240°.

Mössbauer spectroscopy data for the nanosystems based on metallic europium show the opposite results, that is, an increase in the transition temperature of europium. Figure 28 presents the ^{151}Eu Mössbauer spectra of nanostructures **2a**, **2b** and **2c** at T = 90 K recorded upon exposure to shear stress and pressure. The spectrum of nanostructure **2a** (Fig. 28 *a*) exhibits not only four lines of the HFS corresponding to the metallic component (*1* – *4*), but also the europium dioxide and europium oxide lines (*5* and *6*, respectively). Nanostructure **2b** (Fig. 28 *b*) has a

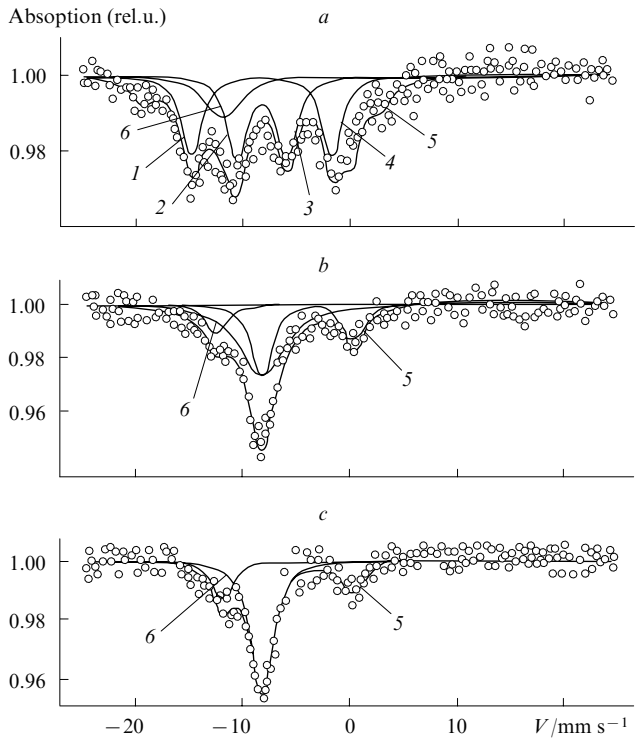


Figure 28. ^{151}Eu Mössbauer spectra of pressure-treated (2 GPa) nanostructures 2.1 (*a*), 2.2 (*b*) and 2.3 (*c*) at $T = 90$ K; the turn angle of anvils was 120°.
For notations *1*–*6*, see text.

triplet spectrum including a broad line from metallic europium and two lines from EuO and Eu_2O_3 (*5*). Nanostructure **2c** also has a triplet spectrum whose components correspond to the magnetic HFS of metallic europium in the magnetically ordered state, a very broad singlet line of metallic europium and a singlet line of EuO (Fig. 28 *c*). The model for magnetic phase transitions in nanostructured systems with defects [86–88] makes it possible to explain all changes observed in the spectra of the oxide and metallic nanosystems.

For iron oxide clusters of size 20–50 nm one should expect first-order magnetic phase transitions. At temperatures above T_C, these clusters lose their magnetisation in jumpwise manner. The critical temperature T_C also depends on the size of the clusters constituting the system. If the cluster size is larger than the critical size R_{cr}, a second-order magnetic phase transition occurs, which is characteristic of bulk samples, and T_C increases. At the same time a decrease in the cluster size ($< R_{cr}$) also leads to second-order magnetic phase transitions due to the decrease in the concentration of defects.

Nanostructuring of iron oxide nanosystems **1a** and **1b** induced by shear stress under pressure leads to a decrease in the average cluster size and average inter-cluster distance. For nanosystem **1a** the effect of the decrease in the cluster size on T_C is compensated by compaction, which causes the magnetic cluster–cluster interaction to strengthen. Nanosystems **1b** and **2b** are only characterised by a decrease in T_C and an increase in the contribution of the first-order magnetic phase transition. This is particularly clearly seen for nanostructure **2b** in which all iron oxide nanoclusters lose magnetic ordering at room temperature. Thus, as the inter-cluster distance increases, magnetic interactions weaken and the first-order magnetic phase transitions become more probable.

The action of shear stress under pressure on metallic europium (sample **2a**) leads to nanostructuring of the material. At temperatures below T_N, the starting metal has a domain structure with domain sizes up to tens of nanometres.[69,89] Above $T_N \approx 80$ K, a first-order magnetic phase transition occurs, accompanied by jumpwise loss of magnetic ordering in bulk metallic europium. In the magnetically ordered state, metallic europium has a domain structure built of nanoclusters packed in the crystal lattice of the metal. If the magnetic nanocluster domains are about 20–30 nm in size, the density of defects is maximum and, as a consequence, the strain responsible for the first-order magnetic phase transitions in metallic europium is also maximum.

This conclusion is confirmed by high magnetostriction coefficients of nanostructured rare-earth metals. The action of shear stress under pressure leads to a decrease in the size of cluster domains ($< R_{cr}$), which causes a decrease in the concentration of defects and strain relief in the metal. As a result, the first-order magnetic phase transition is no longer observed and, as a consequence, the magnetically ordered state is 'pulled' towards higher temperatures and the Néel temperature (T_N) of metallic europium increases. The effect becomes more pronounced upon adding iron oxide clusters (1%) to metallic europium due to higher shear strain of iron oxides compared to metallic europium. This leads to a decrease in the cluster size in the nanostructure. This effect manifests itself to a greater extent after introducing adamantane molecular clusters into the europium matrix. (Adamantane clusters retain the strained state of the nanostructure upon unloading.) In addition, the introduction of impurities (iron oxide clusters and adamantane molecules) seems to favour uniform nanostructuring of samples on exposure to shear stress under pressure. Thus, nanostructuring of magnetostrictors can lead to both a decrease and an increase in T_C (T_N) of nanomaterials.

VI. Thermoelectric materials

Various chemical aspects of research on thermoelectric materials have been reviewed.[90] We will dwell on specific nanomaterials having two-dimensional structure and improved characteristics of heat-to-electricity conversion. The key element of a thermoelectric is a material with unique combination of properties, *viz*., high thermoelectric power, high electric conductivity and low heat conductivity. These properties are determined by the thermoelectric figure of merit

$$ZT = \frac{S^2\sigma}{q}\,T, \tag{21}$$

where S is the Seebeck coefficient, σ is the electric conductivity, q is the heat conductivity and T is the temperature. A more detailed relation is as follows:[91]

$$ZT = \frac{S^2\sigma}{k_L + k_e} = \frac{\sigma}{k_L/\mu\rho e + L_0 T}. \tag{22}$$

Here k_L, k_e are the lattice and electronic components of the hear conductivity, μ and ρ are the mobility and density of carriers and e is charge of electron, $L_0 = 1.5 \times 10^{-8}$ V K^{-2} is the Lorentz constant for semiconductors. This combina-

tion of conducting and heat-conducting properties to fabricate high-performance devices is difficult to attain in a single material.

A schematic of a thermoelectric generator is presented in Fig. 29. After creation of a temperature gradient on the thermoelectric material, charge carriers will move from the hot to cold side and induce a voltage on the load (Seebeck effect). The sign of the coefficient S depends on the sign of charge carriers. Therefore, two modules (one of n-type and one of p-type) with lateral surfaces parallel to the temperature gradient vector and rotated by 45 degrees relative to the direction of electron flow will act as current generator with allowance for summation of the contributions of both modules. This is a principle of operation of thermo-electronic heaters or coolers. Thermoelectric materials should not only be characterised by a high value of the thermoelectric figure of merit (ZT) over a wide temperature range, but also be matched with respect to the degree of n- and p-doping. In addition, the materials the n- and p-moduli are made of should have equal thermal expansion coefficients, exhibit identical changes in the thermal and electrical conductivity, *etc*.

The advantages of thermoelectric devices over conventional sources of cooling or e.m.f. sources are as follows. First of all, these are portability, high reliability (*e.g*., these devices operated on Voyager spacecrafts launched back in 1977), small size and light weight. These devices allow temperature to be controlled locally to an accuracy of 0.1 °C. In addition, there is no need for environmentally hazardous chloro- and fluorocarbons for cooling. Thermoelectric modules can be used as converters of waste heat in, *e.g*., explosions, internal explosion engines, *etc*., which can be useful under energy shortage conditions. Despite considerable advances, the performance of thermoelectric modules is still low; in particular, bulk materials are characterised by $ZT \leqslant 1$ (Ref. 92).

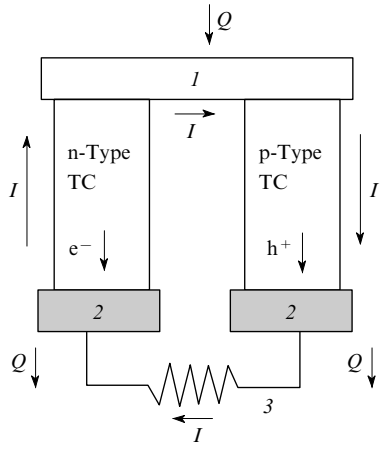


Figure 29. Schematic of a termoelectricity generator.
n- and p-Type thermoelectric cells (TC), matching electrode and terminal electrode (*1*, *2*), load resistor (*3*); '*I*' and '*Q*' denote the directions of the electric current flow and the heat flow, respectively.

Thermoelectric materials considered here represent semiconductor composites with optimal concentration of charge carriers, large effective mass, high charge carrier mobilities, narrow forbidden band and low lattice heat conductivity.[93]

Examples of such materials are provided by Bi_2Te_3, PbTe, $Si_{0.8}Ge_{0.2}$, Zn_4Sb_3. Unlike other electronic materials, which should have a simple structure and in some cases be single crystals, thermoelectric materials are based on heterostructures in, *e.g*., chalcogenides, intermetallics, oxides, *etc*. In this respect, nanomaterials seem to be quite promising. One can assume that, in connection with quantum confinements in nanoclusters, a situation is possible where the density of electronic states at the Fermi level increases, which will lead to an increase in ZT. Another route is to reduce the heat conductivity due to quantum confinement of long-wavelength phonons. To this end, nanoscale superlattices are synthesised on the substrate surface. A superlattice based on Bi_2Te_3/Sb_2Te_3 gave a significant increase in ZT to a value of ~ 2 at room temperature,[91] which confirms the promise of application of nanostructures in thermoelectric modules.

However, thermoelectric materials based on heavy metals are toxic and decompose and undergo melting at high temperatures. In this respect, of considerable promise are metal oxides, in particular, $SrTiO_3$ having a cubic perovskite-type structure and a melting temperature of 2080 °C. In addition, the conductivity of the material can be varied by substituting niobium for titanium. However, a breakthrough in improvement of the efficiency is associated with the use of nanostructured $SrTiO_3$. To this end, we will consider a two-dimensional nanostate called 'quantum well' (the case where the thickness of a nanofilm is smaller than the charge-carrier wavelength)

$$\lambda_{2D} = \frac{h}{\sqrt{3}m^* kT}, \tag{23}$$

where h is the Planck constant, m^* is the effective mass of a conduction electron or hole. The density of states near the bottom of the conduction band or the top of the valence band increases as the depth of the quantum well increases.[94]

An increase in the density of states can lead to an increase in the performance of a thermoelectric module due to an increase in the parameter ZT_{2D} using superlattices.[95] This can be explained by the increase in the Seebeck coefficient owing to an increase in the density of states in the quantum well, whereas the parameters σ_{2D} and k remain unchanged. This model assumes that an increase in S is a consequence of the increase in the density of states near the edge of the conduction band, where the conduction electrons are confined within a narrow domain. The model was partially substantiated taking the system of quantum wells PbTe (1.5 nm)/$Pb_{0.927}Eu_{0.073}$ (45 nm)[96] as an example; the parameter S increased by a factor of 2.5 compared to bulk material.

Conduction electrons are better localised in $SrTiO_3$, because this material is an insulator; one can expect an increase in S and fabrication of efficient two-dimensional thermoelectric. Indeed, an appreciable increase in the Seebeck coefficient was observed for two nanosystems containing a $SrTiO_3$ layer one lattice constant thick (0.39 nm):[97,98] $SrTiO_3/SrTi_{0.8}Nb_{0.2}O_3$ (superlattice) and $TiO_2/SrTiO_3$ (interfaces). The parameters reached in the optimal are $|S| = 850\ \mu V\ K^{-1}$ and $\sigma_{2D} = 1.4 \times 10^3\ S\ cm^{-1}$, which gives $ZT \approx 2.4$. Two-dimensional nanostructures are based on $SrTiO_3/SrTi_{0.8}Nb_{0.2}O_3$ superlattices and $TiO_2/SrTiO_3$ heterolayers. Dielectric $SrTiO_3$ is characterised by the density of conduction electrons $n_e \ll 10^{15}\ cm^{-3}$ (*cf*. $n_e = 2.4 \times 10^{21}\ cm^{-3}$ for $SrTi_{0.8}Nb_{0.2}O_3$ ceramics). These

compounds were deposited on the (001) surface of a $LaAlO_3$ single crystal.

Laser deposition technique was employed in oxygen atmosphere at 900 °C with alternating use of a $SrTiO_3$ (STO) single crystal and $SrTi_{0.8}Nb_{0.2}O_3$ (NSTO) ceramics as targets. The intensity of the maxima of reflections in the case of diffraction of fast electrons could be controlled in the course of deposition of the superlattice layers; this allowed the $SrTi_{0.8}Nb_{0.2}O_3$ layer thickness to be determined precisely (it could vary from 0.5 to 16 lattice constants). The diffraction pattern for X-ray scattering on the $SrTiO_3/SrTi_{0.8}Nb_{0.2}O_3$ superlattice is presented in Fig. 30 *a*. The results of AFM studies of the superlattice are shown in Fig. 30 *b*; here two-dimensional atomic terraces (their height equals the lattice constant of $SrTiO_3$) are clearly seen.

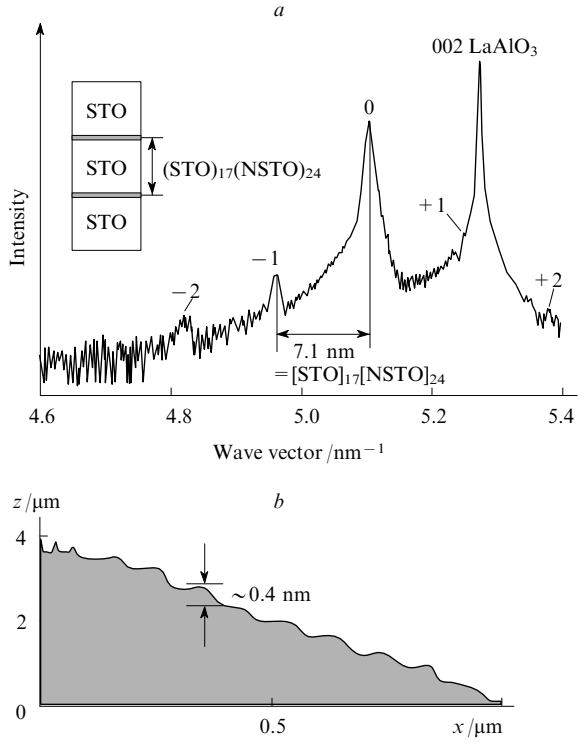


Figure 30. X-Ray diffraction pattern of $(SrTiO_3)_{17}/(SrTi_{0.8}Nb_{0.2}O_3)_{24}$ superlattice grown on the (001) face of a $LaAlO_3$ substrate (satellite peaks are denoted by ±1 and ±2) (*a*) and topographic AFM images of atomically flat terraces and steps on the surface of the superlattice (*b*).[99]

Similar conditions for quantum wells (or two-dimensional electron gas)[99] are met for hetero-interfaces $TiO_2/SrTiO_3$. It is assumed that conduction electrons are localised at the $TiO_2/SrTiO_3$ interface owing to bending of the conduction band of $SrTiO_3$. To verify this assumption, the (001) face of a $SrTiO_3$ single crystal was coated with TiO_2 epitaxial films using laser vaporisation of ceramic rutile. In the oxygen-depleted medium, oxygen-deficient $TiO_{2-\delta}$ films were grown. These films are capable of extracting O^{2-} anions from $SrTiO_3$, thus producing a deficiency in conduction electrons at the $TiO_2/SrTiO_3$ interface. To compare the interfaces, a system 'TiO_2 on the (001) face of a $LaAlO_3$ single crystal' was synthesised.

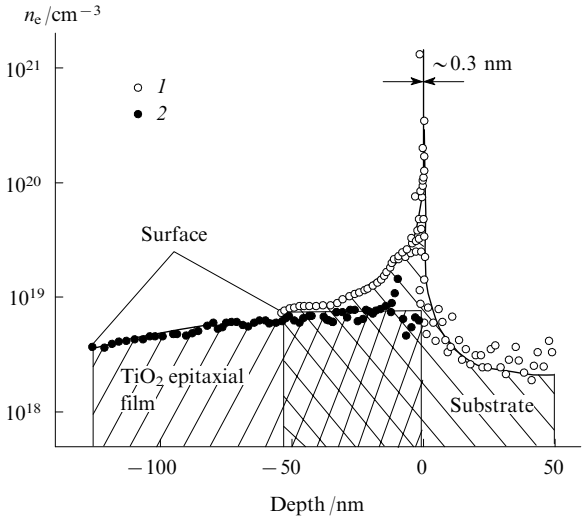


Figure 31. Concentration profiles of conduction electrons in the vicinity of $TiO_2/SrTiO_3$ (*1*) and $TiO_2/LaAlO_3$ (*2*) interfaces.[97]

Figure 31 presents the concentration profiles of conduction electron at the $TiO_2/SrTiO_3$ and $TiO_2/LaAlO_3$ interfaces. In the former case, there is a peak of electron density equal to $n_e \approx 1.4 \times 10^{21}$ cm^{-3}. Its half-width at half-height is ~0.3 nm, which is in agreement with the lattice constant of $SrTiO_3$ (a = 0.39 nm) and corresponds to high density ($n_e \sim 7.0 \times 10^{20}$ cm^{-3}) of electrons localised in a layer one lattice constant thick. At the same time the profile for the $TiO_2/LaAlO_3$ interface gives the electron density $n_e \sim 5 \times 10^{18}$ cm^{-3}. This indicates that no conduction electrons are generated in $LaAlO_3$ and that two-dimensional electron gas is formed only at the $TiO_2/SrTiO_3$ interface.

Now we will consider a key result, *viz*., the dependence of the Seebeck coefficient on the thickness of the $SrTi_{0.8}Nb_{0.2}O_3$ layer in the superlattice. The plot in Fig. 32 shows an abrupt increase in $|S|$ when the layer thickness

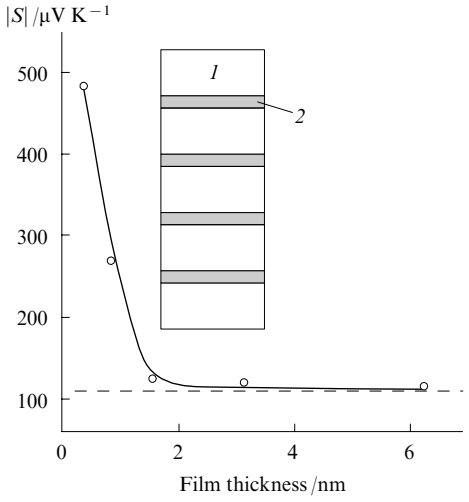


Figure 32. The Seebeck coefficient of $SrTi_{0.8}Nb_{0.2}O_3$ film plotted *vs*. film thickness.[99]
T = 300 K. $SrTiO_3$ layer nine lattice constants thick (*1*) and $SrTi_{0.8}Nb_{0.2}O_3$ layer of thickness one, two, four, eight and sixteen lattice constants (*2*).

becomes less than 1.56 nm (or four lattice constants). For a layer one lattice constant thick one has $|S,| = 480$ μV K^{-1}. This is 4.4 times larger than for bulk $SrTi_{0.8}Nb_{0.2}O_3$ ($|S| = 108$ μV K^{-1}).

It is interesting to analyse the parameters ZT for a thin film (two-dimensional electron gas.) Figure 33 presents the dependences of this parameter on the carrier concentration for two-dimensional nanostructure (two-dimensional electron gas), bulk $SrTiO_3$ and a nanostructure composed of nine unit cell barrier layers. The parameter $ZT_{2D} = 2.4$ is 24

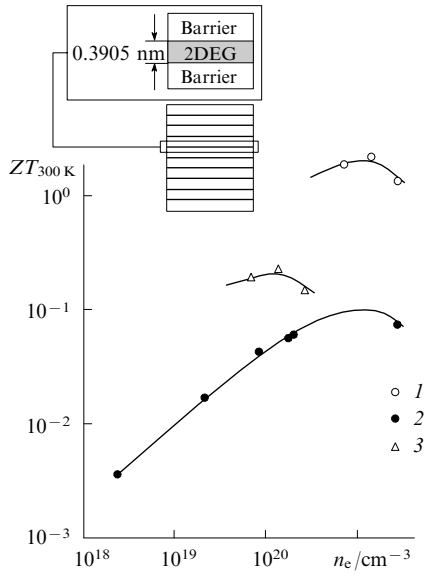


Figure 33. Thermoelectric figures of merit $ZT_{300\,K}$ plotted *vs.* carrier concentration for two-dimensional electron gas (*1*), bulk $SrTiO_3$ (*2*) and a system composed of nine unit cell barrier layers (*3*) at 300 K.[99] '2DEG' stands for 2D electron gas.

times higher than for bulk $SrTiO_3$ ($ZT_{300\,K} = 0.1$). Since the electric conductivity of the barrier layers confining the conduction band is lower than that of the two-dimensional layer, the effective conductivity (σ_{ef}) is proportional to the total thickness of the barrier.

$$\sigma_{ef} = \frac{\sigma_{2D}}{1 + N_b}. \tag{24}$$

Then one has

$$ZT_{ef} = \frac{ZT_{2D}}{1 + N_b}, \tag{25}$$

where N_b is the number of two-dimensional nanostructures separated by the $SrTiO_3$ barriers, which confine the conduction band of the two-dimensional nanostructures.[100]

VII. Chemoelectrics

Now we will consider examples of application of nanomaterials in energy-saving devices,[101, 102] in particular, in the most efficient lithium cells. These nanosystems are consituents of new-generation energy-saving devices characterised by high power, high density of energy stored and high charging–discharging current, which is necessary for production of electric vehicles. A lithium cell includes a positively charged lithium-containing electrode ($LiCoO_2$) and a negative electrode (graphite). In the course of charging, lithium ions are extracted from $LiCoO_2$ and intercalated into the graphite electrode. Discharging is accompanied by reversible extraction of lithium ions from the carbon matrix and transfer to the positively charged electrode. It is desired that the energy stored on intercalation of lithium ions and related to their mass or volume be maximum. To compare the energy stored, the notion 'specific energy density' measured in W h kg^{-1} or W h litre^{-1} is introduced; the energy release rate is measured in W litre^{-1}. In conventional lithium cells the specific energy density can be as high as 50 W h kg^{-1}. To improve this parameter, nanostructured electrodes are used, as well as novel chemical reactions that cannot occur in bulk materials; the surface area of the electrode/electrolyte contact increases, which leads to acceleration of the charging–discharging process and shortening of the ion and electron transfer distances, *i.e.*, one can consider the operation at low ionic or electronic conductivity.

Positive electrodes for novel efficient lithium cells are based on transition metal oxide, sulfide, fluoride and nitride nanoparticles.[103]

Charging–discharging involving transition metal compounds causes the formation of nanoparticles intercalated into the Li_nX (X = O, S, F, N) matrix. Transition metals do not form alloys with lithium. The process for bulk electrodes containing lithium alloys can be described as follows:

$$M + x\,Li^+ + x\,e^- \rightleftharpoons Li_xM,$$

where M = Sn, Si, Pb, Bi, Sb, Ag, Al or a multicomponent alloy. In nanostructured electrodes based on transition metals, charging and discharging of the cell are accompanied by oxidation and reduction of metallic nanoclusters at the positive electrode. The mechanism is described by the equation

$$MX + z\,Li^+ + z\,e^- \rightleftharpoons Li_xX + M,$$

where M is the transition metal (Fe, Co, Ni, Cu, *etc.*) cluster.

Using processes with participation of clusters, high specific capacitances of lithium cells were obtained, namely, up to 700 mA h g^{-1} for 100 charging–discharging cycles at fast discharging and voltages in the range of 3.5–0.01 V.[104]

High capacitance of a cell with electrodes containing transition metal oxide clusters is due to charge accumulation at interfaces.[105, 106] According to this model, lithium ions are accumulated at the oxide side of the interface, whereas electrons are localised at the metallic surface of the nanocluster, *i.e.*, charge separation occurs. The size effects of the electronic conductivity of the metallic cluster enhance the electrochemical activity towards formation–decomposition of Li_2O. Namely, as the cluster size decreases, the number of surface atoms increases, thus leading to an increase in electrochemical activity. This fact, in particular, provides an explanation for the dependence of the repeatability of the charging discharging cycles on possible aggregation.

Nanostructuring of electrodes is not only the reason for novel cluster reactions, but also favours improvement of the electrochemical properties of the charger, *viz.*, an increase in the specific capacitance, the charging–discharging current and enhancement of the cyclic stability. This is a conse-

quence of the shortening of the diffusion path length for intercalation of lithium ions and an increase in the surface area of contacts between the active surfaces and electrolyte.

As an example we will consider bulk and nanocrystalline rutile (TiO_2). At room temperature, bulk rutile can contain lithium ions as minor impurity.[107] Diffusion of lithium ions in rutile occurs anisotropically, mainly along the *c* axis, whereas diffusion in the *ab* plane is slow and thus precludes the occupation of octahedral sites by lithium ions. In the nanocrystalline state, the situation changes. For instance, the proportion of lithium ions in 15-nm rutile nanoclusters is high ($x > 1$ in Li_xTiO_2)[103] due to shortening of the diffusion path length for intercalation of lithium ions and an increase in the specific surface area.

Electrode/electrolyte contacts are also of great importance. It is interesting to study the effect of the specific surface area of electrodes on the cell capacitance and the charging–discharging current. When comparing two factors, the shortening of the diffusion path length for intercalation of lithium ions accompanied by an increase in the charging–discharging current and the increase in the specific surface area, the latter factor predominates because the surface area of the cluster/electrolyte interface is of crucial importance for the increase in the cell capacitance. Using nanoelectrodes with a large specific surface area, one can considerably reduce the specific current density,, which allows stable operation and high capacitance of the cell to be maintained. For instance, CoO-based nanoelectrodes are characterised by recovery of 85% of the initial capacitance at a charging–discharging rate of $2C$ (C is the rate necessary for charging–discharging a certain theoretical capacitance over a period of 1 h).[103] High specific capacitance, charging rate and cyclic stability were observed for TiO_2 (Ref. 108) and $Li_4Ti_5O_{12}$ nanoelectrodes.[109]

Spinel-type $Li_4Ti_5O_{12}$ electrodes appeared to be particularly efficient because the intercalation and extraction of lithium atoms occurs with a small change in volume, which ensures a high cyclic stability. Nanocrystalline $Li_4Ti_5O_{12}$ electrodes show a high performance with respect to intercalation of lithium ions even at a charging rate of $250C$.[109]

The results of a study of the charging voltage on the charging capacitance at different charging–discharging currents for a 6-nm anatase nanocluster are presented in Fig. 34 (see Ref. 103). A decrease in the size of TiO_2 nanoclusters on electrodes led to a slower rate of the decrease in the length of the plateau in the plot. The character of the charging–discharging curves was only slightly dependent on the discharging current, which is confirmed by good cyclic dependence of the cell capacitance (Fig. 34 *a*).

Ion–electron transport plays an important role in chemical reactions. Reduction reactions in nanostructured electrodes are accompanied by transfer of lithium ions and electrons. The shortest path lengths and the highest current are provided by nanoclusters and nanopores in electrodes.

Diffusion of lithium ions is a complex process and depends on the nanopore size. One can consider a simple model with the diffusion path length given by

$$L = \sqrt{Dt},$$

where D is the diffusion coefficient and t is the duration of diffusion. At the same time, by definition the specific capacitance of a cell is

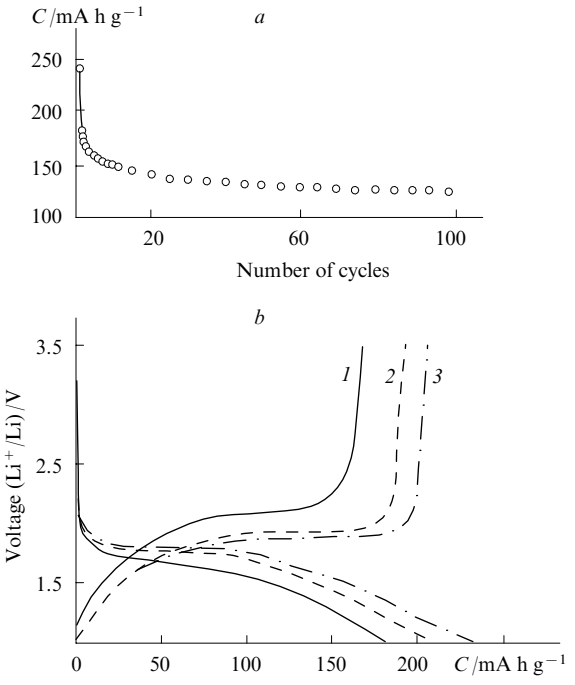


Figure 34. Cyclic charging–discharging stability (*a*) and the dependence of the charging voltage on the capacity for nanostructured anatase (TiO_2) electrodes at a specific charging–discharging current of 10 (*1*), 1 (*2*) and 0.1 (*3*) A g^{-1} (*b*).[103]

$$Q = It,$$

where I is the specific current density (in A kg^{-1} or mA g^{-1}). For a certain (specified) capacitance an increase in electric current leads to shortening of the charging time. The effective specific capacitance is determined by the ratio of the diffusion path length to the nanocluster size

$$C_{ef} = \frac{r^3 - (r - L)^3}{r^3},$$

where r is the radius of the nanosystem. From this relation it follows that, to obtain a maximum specific density, the parameter L should be larger than r. Assuming that charging–discharging takes 1 min and the diffusion coefficient for a solid is 10^{-16} cm^2 s^{-1}, the cluster size should be about 2 nm. These estimates are quite realistic for nanoporous TiO_2 with two-dimensional hexagonal mesostructure with 4-nm pores and 5-nm pore wall of nanocrystalline anatase. These nanostructured electrodes are characterised by a specific capacitance of 260 mA h g^{-1} at high current density (10 C g^{-1}). Similar results were also obtained for 6-nm TiO_2 nanocrystals.[103]

Long-term cyclic operation of a cell also requires the shortest path length of electrons participating in the charging–discharging process. To improve the conductivity, carbon black is used as an additive. For better electrode/carbon contact, electrode materials, such as V_2O_5,[110] TiO_2 (Ref. 111) and MnO_2,[112] contain acetylene carbon black.

Combined nanoelectrodes with electronic conductors in the form of nickel microgrid coated with mesoporous nanooxide layers NiO, Fe_2O_3 and Co_3O_4 (Fig. 35) seem to be quite promising.[113–116]

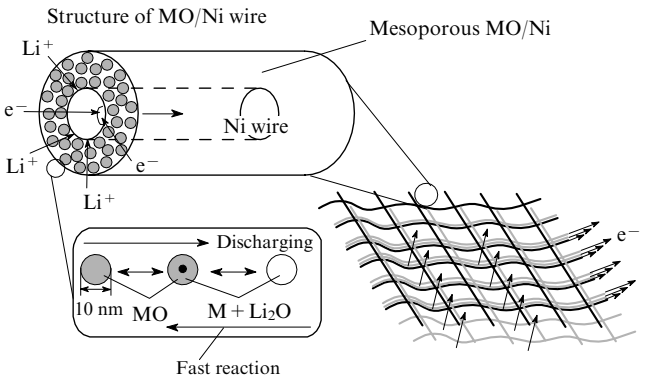


Figure 35. Schematic of a composite fragment of nickel lattice. Core: nickel wire; sheath: mesoporous oxide. Arrows denote the directions of electronic and ionic conduction on charging–discharging.[113] M is metal.

Metal oxide nanoclusters localised in mesopores are oxidised in the course of discharging and reduced during the charging of the cell. Nanosystems NiO–Ni and Fe_2O_3–Ni are characterised by high capacitance, *viz.*, 695 mA h g^{-1} at a discharging current of 10 A g^{-1} and 780 mA h g^{-1} at 13 A g^{-1}, respectively. Figure 36 presents the charging-discharging dependences for the nanosystem Fe_2O_3–Ni.[114]

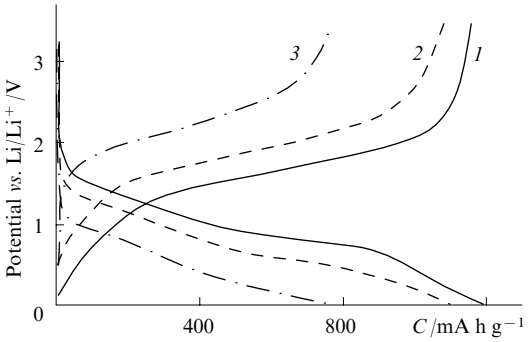


Figure 36. Potential-*vs.*-capacity curves for electrode nanosystem Fe_2O_3–Ni at a specific charging–discharging current of 0.78 (*1*), 7.3 (*2*), 13 (*3*) A g^{-1} (see Ref. 14).

In addition to high and stable charging–discharging current, cyclic stability is of great importance. A decrease in the cell capacitance is usually associated with changes in the electrode volume owing to expansion and compression in the course of intercalation and extraction of lithium ions. For instance, a negative silicon electrode has the highest theoretical capacitance of 4200 mA h g^{-1} (Ref. 117). However, abrupt changes in its volume causes cracking and thus the loss of cyclicity. Nanostructured materials can absorb a necessary volume without violation of its integrality. For instance, Si/C nanostructured composite electrodes exhibit a very high reproducible capacitance ($\sim$1000 mA h g^{-1}) and high cyclicity.[118]

VIII. Metamaterials

'Metamaterials' is the common name of ordered systems comprised of individual elements having a negative refractive index of microwave radiation[119] and simultaneously negative values of magnetic permeability and dielectric permittivity. The synthesis of metamaterials to a great extent confirmed theoretical predictions of the possibility of existence of materials with such properties, which were made by Veselago[120] more than four decades ago. Negative refractive indices were observed for metamaterials in the radiofrequency,[121] microwave,[119] the far and near IR,[122, 123] and in the visible region,[123] *i.e.*, in the frequency range spanning from mega- to terahertz.

1. Interaction of electromagnetic radiation with materials. Magnetic and electric interactions

Prior to considering particular examples of application of nanomaterials as metamaterials, it is appropriate to analyse some common properties of metamaterials and their changes under the action of electromagnetic radiation. To this end, we will consider two parameters of a homogeneous medium assuming that the wavelength of radiation is longer than the (i) characteristic size of the element of a metamaterial and (ii) distances between these elements:
dielectric permittivity

$$\varepsilon(\omega) = \varepsilon_1(\omega) + i\varepsilon_2(\omega), \quad (26)$$

magnetic permeability

$$\mu(\omega) = \mu_1(\omega) + i\mu_2(\omega), \quad (27)$$

where ω is the frequency of electromagnetic radiation. These quantities participate in the formation of the conductivity and absorption of radiation. The refractive index is determined from the relation

$$n(\omega) = \varepsilon(\omega)\mu(\omega). \quad (28)$$

This parameter makes it possible to measure the deviation of a beam of radiation when it passes through an interface between two media with different refractive indices. The interrelation between the refractive indices is known as Snell's law[124]

$$n_1 \sin\theta_1 = n_2 \sin\theta_2, \quad (29)$$

where n_1, n_2 are the refractive indices of the first and second medium, respectively, and θ_1, θ_1 are the angles of refraction (angles between the direction of beam propagation and the normal to the interface).

The schemes of transmission of a beam of radiation issuing from a point source through plates made of the positive ($n = 1.5$) and negative ($n = -1$) refractive index materials are shown in Fig. 37. The angles of refraction of the beam are determined using Eqn (29). In addition, changes in the relative intensity of the absorbed component of radiation are shown. As can be seen, the negative refractive index material enable fabrication of lenses with a unique short focussing range.[125]

Consider separately the magnetic and electric elements responsible for creation of negative values of ε and μ.

2. The magnetic element

Negative values of magnetic permeability are attained using inductive (L)-capacitive (C) magnetic LC-resonators (a kind of 'magnetic atom') proposed by Pendry.[126] They are used to form an ordered three-dimensional array. The magnetic

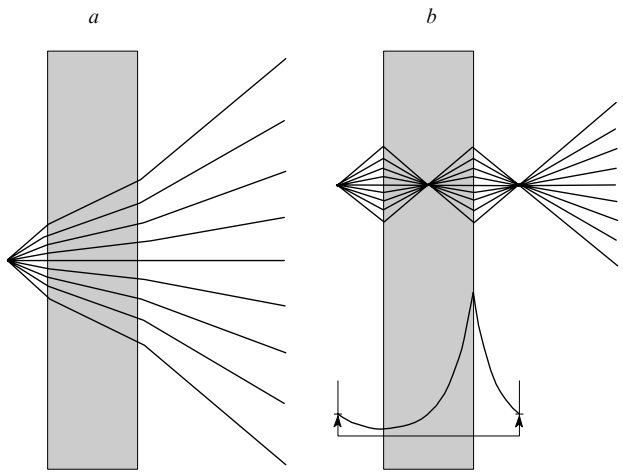


Figure 37. Schematic of transmission of radiation from a point source through plate made of a positive ($n = 1.5$) (*a*) and negative ($n = -1.0$) (*b*) refractive index material.
Changes in the relative intensity of incident radiation with the sample thickness are shown in bottom right.

element and its electric circuit are shown in Fig. 38.[127] The magnetic element is called a split resonance ring, or SRR; this abbreviation is most often used. Alternating magnetic field normal to the SRR plane induces an electric current

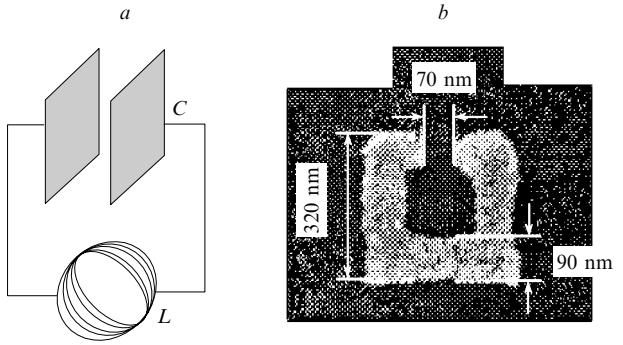


Figure 38. Electrical circuit of a magnetic structure (*a*) and an electron micrograph of actual structure (*b*) with a resonance in the 80–90 THz region (wavelength ~ 3.5 μm).[127]

and causes accumulation of electric charge at the electric circuit break as in the capacitor *C*. Thus, a SRR is an *LC*-circuit with the resonance frequency

$$\omega_0 \sim \sqrt{\frac{1}{LC}},$$

where the inductance *L* is due to the conducting fragment of the SRR. At alternating magnetic field frequencies lower than ω_0, the current flowing in the SRR is due to this field and one deals with a positive magnetic permeability. But as the frequency increases, lagging current flows in the SRR, which leads to a negative value of μ. The effective magnetic permeability of the SRR is given by[128]

$$\mu_{\mathrm{ef}}(\omega) = 1 + \frac{F\omega^2}{\omega_0^2 - \omega^2 - \mathrm{i}\Gamma\omega}, \tag{30}$$

where *F* is the geometric factor, ω_0 is the resonance frequency and Γ is the damping constant.

3. The electric element

If the frequency of radiation is lower than the plasmon frequency (ω_{p}), all metals have negative values of dielectric permittivity, which is due to screening of electromagnetic radiation by free electrons. One can create an ordered array of metallic elements, *e.g.*, straight metallic wires, truncated segments or loops.[129] The frequency dependence of dielectric permittivity is given by[123]

$$\varepsilon(\omega) = 1 - \frac{\omega_{\mathrm{p}}^2}{\omega_0^2 - \omega^2 + \mathrm{i}\omega\Gamma}, \tag{31}$$

where

$$\omega_{\mathrm{p}}^2 = 4\pi\frac{ne^2}{m^*}, \tag{32}$$

$$\omega_0 \approx \frac{\omega_{\mathrm{p}}}{\sqrt{3}}.$$

Since the charge carrier density (*n*) can be considerably reduced for thin wires while the effective mass (m^*) of charge carriers can, on the contrary, be increased, the effective plasmon frequency can be reduced by a few orders of magnitude; this makes a medium with $\varepsilon < 0$ possible.

4. Negative refractive and reflection index metamaterials

Combining magnetic and electric elements with negative values of μ and ε (more exactly, μ_1 and ε_1) allows one to design a single material with a negative value of refractive index ($n < 0$). This will cause changes in many electromagnetic phenomena,[120] *e.g.*, a change in the direction of the phase velocity of the Doppler shift of the source relative to the absorber, Cherenkov radiation, converging lenses become diverging ones, *etc*.

The negative refractive index was for the first time reported for a composition of SRR and metallic wires in the microwave region.[130] Metamaterials operating in the megahertz, microwave, millimetre, terahertz and visible frequency regions have also been designed.[121–123]

An SRR array (single SRR is shown in Fig. 39) exhibited negative values of dielectric permittivity and magnetic permeability in the terahertz region.[127] A square periodic array with a lattice constant $a = 450$ nm included a total of $56 \times 56 = 3136$ elements. The structure was made of gold foil and patterned using electron-beam lithography. Negative values of ε_1 and μ_1 in the vicinity of resonance are determined by the direction of electromagnetic wave propagation relative to the SRR, *i.e.*, to the directions of the electric field vector $\boldsymbol{E}$, magnetic field vector $\boldsymbol{H}$ and the wave vector $\boldsymbol{k}$. Plasmon resonance and negative values of ε_1 arise when electric current flows along the SRR base parallel to the vector $\boldsymbol{E}$ (Fig. 39 *a*). Magnetic *LC*-resonance and negative values of μ_1 are related to the magnetic field direction normal to the SRR.

Miniaturisation of SRR causes the appearance of new resonances, which differ from conventional magnetic and plasmon resonances.[123] This nanometamaterial represented an array of gold SRRs with a minimal characteristic size of 50 nm. The SRR array was patterned using conventional electron beam lithography on a glass substrate covered with a 50-nm layer of indium–tin oxide to remove charge from the poly(methyl methacrylate) substrate during the expo-

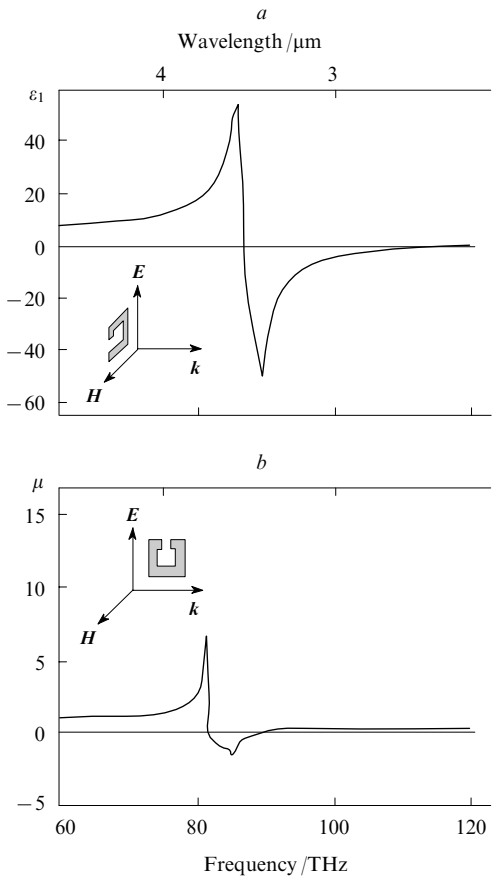


Figure 39. Frequency dependences of the real part of dielectric permittivity (*a*) and magnetic susceptibility (*b*).[127]
Shown are the arrangements of the SSR structure and the directions of the vectors ***E***, ***H*** and ***k***.

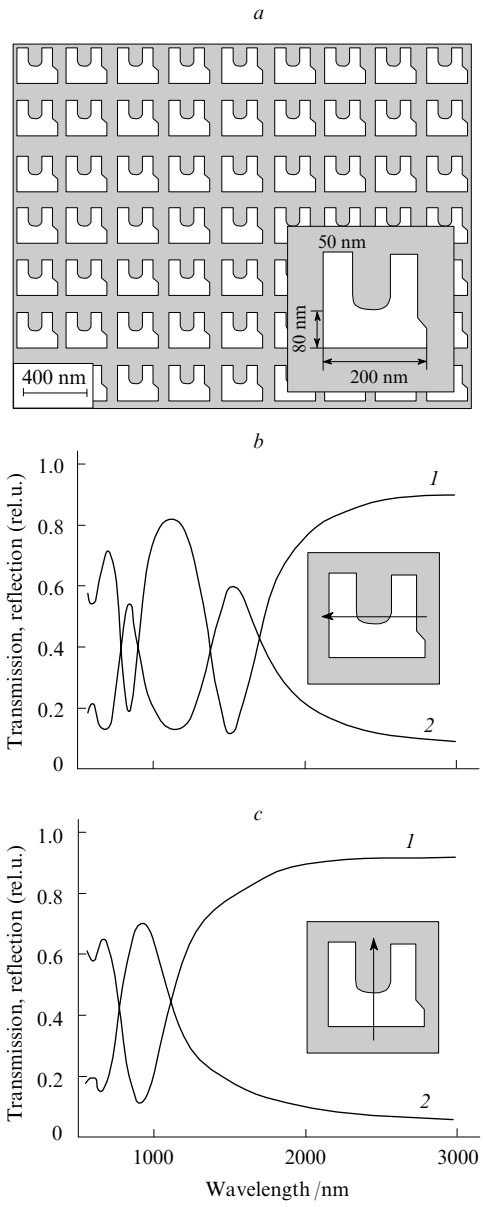


Figure 40. Electron micrograph of the lattice and a schematic of an SSR structure (inset: SSR structure and its dimensions) (*a*) and the transmission (*1*) and reflection (*2*) spectra obtained at different orientation of the vector of the electric field polarisation relative to the SSR structure (*b*, *c*).[123]

sure. A single SRR and the SRR array are shown in Fig. 40 *a*. Figures 40 *b*,*c* present the IR Fourier transmission and reflection spectra for radiation propagating normal to the SRR array plane but having different orientations of the electric polarisation vector. Figure 40 *b* shows a characteristic magnetic resonance at 1500 nm, which disappears at another polarisation of radiation (Fig. 40 *c*); only the plasmon resonance is observed in the latter case. However, the plasmon frequency differs from that calculated using relations (30) and (32), being intermediate between 950 and 800 nm. This shift is due to the appearance of new vibrational modes.[123]

When the electric field of the beam interacts with the metamaterial, electric charge is accumulated on the surfaces of the vertical plates of the SRR, which causes depolarisation of radiation. This depolarisation can enhance or reduce the external electric field. In addition to the resonances at 950 and 800 nm a plasmon resonance at 600 nm is also observed, which is due to the depolarisation field of the short axis, *i.e.*, by the width of the SRR. For horizontal polarisation is excited a resonance associated with the lower bar of the SRR. For vertical polarisation the contribution to resonances comes from two vertical segments of the SRR. Coupling of the two modes gives rise to two new vibrational modes, a symmetrical (with a reduced frequency) and antisymmetrical (with a higher frequency compared to the frequency of single-mode plasmon resonance). Under normal-incidence conditions, the antisymmetrical mode is not excited (owing to zero electric dipole moment), whereas the symmetrical mode is excited, which leads to the overall shift of the resonance.

Thus, investigations of this metamaterial revealed the *LC*-resonance at ~1500 nm with a negative μ value and the plasmon resonance, for which the frequency shift depends on the polarisation of radiation and on the appearance of new vibrational modes in the SRRs.

Yet another metamaterial[131] represents a layered nanostructure comprised of two metallic gold films 30 nm thick separated by an Al_2O_3 dielectric layer 60 nm thick. The nanostructure forms a square array of through cylindrical orifices 360 nm in diameter; the 'lattice constant' is 838 nm (Fig. 41).

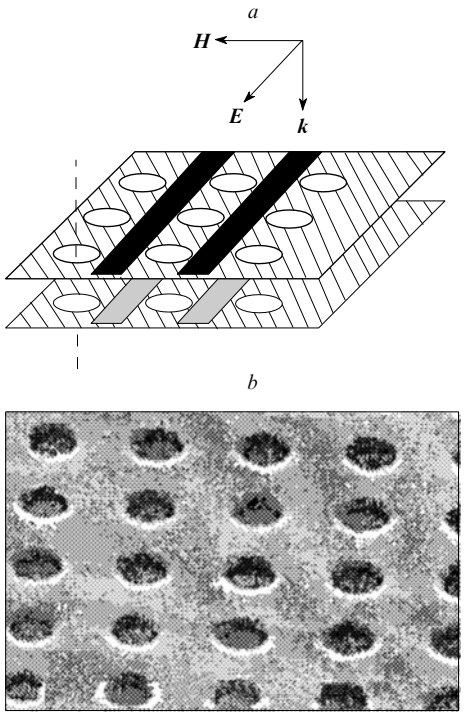


Figure 41. A circuit (*a*) and a SEM image (*b*) of a junction composed of Au layers and an Al_2O_3 layer with orifices forming a square grid.[131] Shown are the electromagnetic wave vectors and the wave vector (*a*): to denote the polarisation and the directions along which the fields act, the electric field affected regions are shown in dark and the magnetic field affected regions are shaded; the SEM image (*b*).

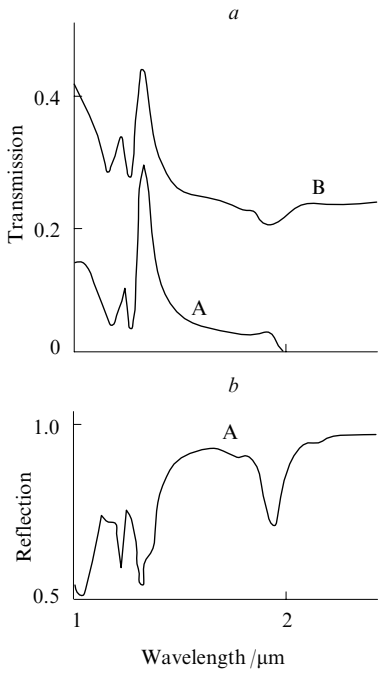


Figure 42. Transmission (*a*) and reflection (*b*) spectra of the metamaterials A and B (see text).[131]

The nanostructure can be treated as consisting of two functional fragments. The magnetic component of radiation interacts with the dashed regions. The upper and lower metallic foils form an inductive circuit, where the induced current is broken by the orifice, which plays the role of a capacitor, *i.e.*, an *LC*-resonator is thus formed. In the vicinity of resonance, this fragment of the nanoarray induces an antiparallel field with respect to the incident one; this causes the magnetic permeability to decrease and leads to negative values of μ. Dark metallic regions absorb the electric field under plasmon resonance conditions and correspond to negative values of ε.

To determine the refractive indices of radiation, one should measure the amplitudes and phases of the transmitted and reflected radiation. To this end, nanostructures for interferometric determination of the phase of transmitted or reflected radiation were synthesised in addition to the main nano-array A shown in Fig. 41. In particular, sample B contained strips of metamaterial on glass substrate, separated by strips of free space to reduce the absorption of radiation and to create prerequisites for three-dimensional interference.

The absorption and reflection spectra of samples A and B recorded with an IR Fourier spectrometer are shown in Fig. 42. The spectra exhibit a clearly seen peak at 1.3 μm, originating from plasmon resonance at the glass – Au interface. Yet another plasmon resonance at a somewhat longer wavelength originates from the Al_2O_3/Au interface. The resonance at 2 μm is the magnetic *LC*-resonance, as in the case of SRR. Using experimentally measured amplitudes and phases of transmitted and reflected radiation, one can determine the complex refractive index and thus its real and imaginary parts.

The real part of the refractive index has negative values and a minimum equal to about -2 near $\lambda = 2$ μm, whereas the imaginary part is strongly modulated and exceeds a value of 3 in the vicinity of resonance. This suggests a strong absorption of the metamaterial due to electron scattering by thin metallic films.

Yet another nanometamaterial[132] is much far from the artificial materials used for fabricating SRR arrays. This is a superlattice comprised of thin superconducting and ferromagnetic layers. In this nanomaterial the high-temperature superconducting layers $YBa_2Cu_3O_7$ (YBCO) provide a negative dielectric permittivity while ferromagnetic layers of dielectric manganite $La_{0.89}SrO_{0.11}MnO_3$ (LSMO) provide a negative magnetic permeability in the vicinity of ferromagnetic resonance. The superlattice was fabricated by deposition of YBCO and LSMO layers on the substrate $(LaAlO_3)_{0.3}(Sr_2LaAlTaO_6)_{0.7}$ (LSAT) under high pressure. The formation of the superlattice was monitored by X-ray diffraction analysis and magnetic measurements using a magnetometer. Figure 43 presents the temperature dependences of the magnetic susceptibility in external magnetic field switched on and off. Magnetisation measurements gave $T_C \approx 207$ K and the saturation magnetisation $M_{LSMO} = 1.5\ \mu_B$. The magnetic field dependences of the absorption amplitude and phase shift of the superlattice YBCO/LSMO were studied in the terahertz frequency range. In Fig. 44 we present the magnetic field dependences of the transmission and phase shift at 90 GHz. A ferromagnetic resonance near 3.1 T was observed. As the temperature is raised above 200 K, the resonance disappears.

Ferromagnetic resonance lines can be calculated assuming a Lorentzian lineshape and a complex magnetic permeability in the form

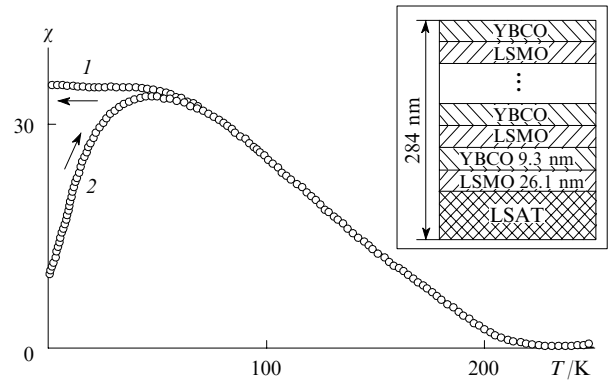


Figure 43. Magnetic susceptibility of nanolayered superlattice YBCO/LSMO at magnetic field switched on (*1*) and off (*2*).
The inset shows the dimensions and the arrangement of the layers in the superlattice.[132]

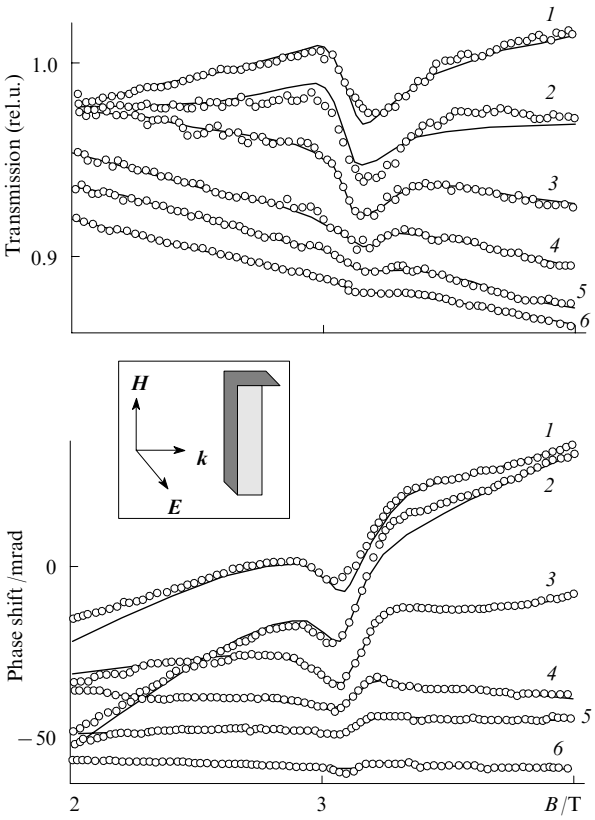


Figure 44. Magnetic field dependences of the absorption and phase angle at 90 GHz for an YBCO/LSMO superlattice at different temperatures.[132]
Theoretical curves (solid lines) were obtained using relation (33). The inset shows the orientation of the superlattice relative to the direction of radiation. T/K: 10 (*1*), 40 (*2*), 70 (*3*), 90 (*4*), 150 (*5*) and 200 (*6*).

$$\mu = \mu_1 + \mathrm{i}\mu_2 = 1 + \frac{\Delta\mu H_0 H}{H^2} - H_0^2 - \mathrm{i}H\Gamma, \qquad (33)$$

where H_0, Γ and $\Delta\mu$ are the resonance field, the width of the resonance and the magnetic contribution to the ferromagnetic resonance line, respectively. For the resonance in question one has $\Gamma = 0.2 \pm 0.02$ T.

At $T > 90$ K, the following relation is valid for a ferromagnetic

$$\Delta\mu \sim \frac{M}{H_0},$$

where $\Delta\mu(90\mathrm{K}) = 0.4$, $\Delta\mu(200\mathrm{K}) = 0.2$. At temperatures lower than the temperature of transition to the superconducting state, the transmission intensity decreases owing to possible screening. The ferromagnetic resonance lineshapes for the metallic and superconducting states are strongly different, being symmetrical (*e.g.*, at $T = 90$ K) in the former and asymmetrical (*e.g.*, at $T = 10$ K) in the latter case.

Intense ferromagnetic mode in the superconducting state causes a negative magnetic permeability in the vicinity of resonance. At the same time the real part of the dielectric permittivity of the superconductor, $\mathrm{Re}(\varepsilon) = \varepsilon_1$, is also negative. Thus, in this case the system can exhibit a negative refractive index. The magnetic permeability and refractive index calculated from the data shown in Fig. 44 are presented in Fig. 45. The ferromagnetic resonance mode is responsible for negative magnetic permeability in the magnetic fields 2.9 – 3.1 T (see Fig. 45 *a*). Combining with negative values of dielectric permittivity for the superconductor gives

$$\varepsilon(10\ \mathrm{K}) = (-13.7 + 6.1\mathrm{i}) \times 10^4.$$

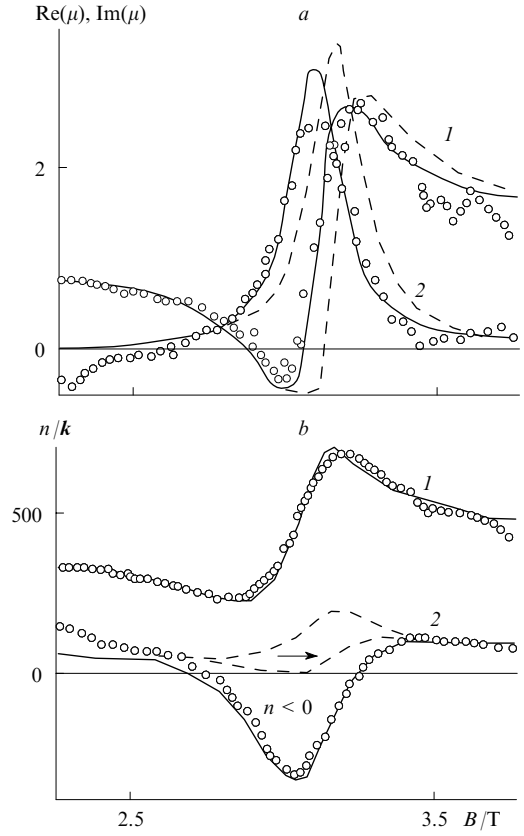


Figure 45. The magnetic susceptibility of an YBCO/LSMO superlattice (*a*), the wave vector and the refractive index (*b*) plotted *vs.* magnetic field.[132]
$T = 10$ K; dashed lines denote the dependences at 200 K. (*a*): $\mathrm{Re}(\mu)$ (*1*), $\mathrm{Im}(\mu)$ (*1*); (*b*): (*1*) $\boldsymbol{k}$, (*2*) n.

This is the reason for the appearance of a large region with negative refractive index (see Fig. 45*b*). For comparison, Fig. 45*b* presents the n values at $T = 200$ K; they are positive.

Thus, negative values of the refractive indices can be obtained using a superlattice comprised of superconducting and ferromagnetic layers in the vicinity of ferromagnetic resonance; transition from positive to negative values of n is magnetically controlled.

5. Metamaterials: promising fields of application

As emphasised above, negative values of refractive index are exhibited near some resonance frequency ω_0, which is determined by the geometry of the SRR or other elements constituting the metamaterial. This should be used in the design of frequency-tunable metamaterials. For SRR the resonance frequency is given by [126]

$$\omega_0 = \frac{\sqrt{3}}{\pi\mu_0 C r^3}, \tag{34}$$

where r is the radius of the SRR ring, μ_0 is the static magnetic permeability and C is the capacitance per unit surface area between two rings.

Thus, the frequency can be varied by varying not only the size of the element, but also the capacitance, which is determined by the dielectric constant of the medium.

Dynamic tuning of resonance absorption of SRRs was done [133] using a GaAs semiconductor matrix. A 50-fs pulse at 800 nm excited a photocurrent through the forbidden band of the semiconductor. Since photo-induced charges have a relatively long lifetime (1 ns), the states of the SRR can be studied in the terahertz range. Photoconductivity, which arises in the matrix, suppresses the low-frequency resonance at $\omega_0 = 0.5$ THz, which is due to magnetically induced circulation of current, and has no effect on the plasmon resonance at 1.6 THz. This is an example of how the hybrid metamaterial can be used as a switch in the terahertz frequency range.

The second field of application of metamaterials is the design of nanostructures including superlattice or nanocluster crystals for magnetic and electric (plasmon) resonances in the near-IR or visible regions. A possible example is a dielectric matrix containing magnetodielectric spherical particles.[134]

* * *

Going from bulk materials to heteronanostructures, as well as the use of interfaces and superlattices considerably increase the potential of control of the magnetic and electric properties. Nanocontrollers fabricated for operating in weak magnetic and electric fields at ambient temperature will find application in many fields from healthcare and biology to large-scale production of various items.

This review has been written under financial support from the Russian Foundation for Basic Research (Project No. 09-03-00023).

References

1. A I Gusev *Nanomaterialy, Nanostruktury, Nanotekhnologii* (Nanomaterials, Nanostructures and Nanotechnologies) (Moscow: Fizmatlit, 2007)
2. I P Suzdalev *Fizikokhimiya Nanoklasterov, Nanostruktur i Nanomaterialov* (Physical Chemistry of Nanoclusters, Nanostructures and Nanomaterials) (Moscow: Komkniga, 2006)
3. L D Landau, E M Lifshits *Elektrodinamika Sploshnykh Sred* (Electrodynamics of Continua) (Moscow: Gos. Izd. Tekhniko-teoret. Lit., 1957) p. 119
4. G A Smolenskii, I E Chupis *Usp. Fiz. Nauk* **137** 415 (1982) [*Physics-Uspekhi* **25** 475 (1982)]
5. J P Rivera, H Schmid *Ferroelectrics* **161** 91 (1994)
6. H Schmid *Int. J. Magn.* **4** 337 (1973)
7. Yu F Popov, A M Kadomtseva, G V Vorob'ev, V A Sanina, A K Zvezdin, M M Tehranchi *Physica B* **284–288** 1402 (2000)
8. Yu F Popov, A M Kadomtseva, S S Krotov, D V Belov, G P Vorob'ev, P N Makhov, A K Zvezdin *Low-Temp. Phys.* **27** 478 (2001)
9. T Kimura, S Kawamoto, I Yamada, M Azuma, M Takano, Y Tokura *Phys. Rev. B* **67** 180401 (2003)
10. L N Baturov, B I Al'shin, Yu N Yarmukhamedov *Fiz. Tv. Tela* **20** 1300 (1978) [a]
11. J F Scott *Rep. Prog. Phys.* **12** 1065 (1979)
12. T Katsufuji, S Mori, M Masaki, Y Morimoto, N Yamamoto, H Takagi *Phys. Rev. B* **64** 104419 (2001)
13. J Wang, J B Neaton, H Zheng, V Nagarajan, S B Ogall, B Lin, D Viehland, D Viehland, D C Shiom, V Vaithyanathan, D G Shiom, U V Wagmari, N A Spaldin, K M Rabe, M Wuttig, R Ramesh *Science* **299** 1719 (2003)
14. E Acher, H Rieder, H Schmid, H Stossel *J. Appl. Phys.* **37** 1404 (1966)
15. I N Baturov, B I Al'shin, Yu N Yarmukhamedov *Fiz. Tv. Tela* **20** 2254 (1978) [a]
16. J F Scott *Rep. Prog. Phys.* **12** 1056 (1979)
17. M Fiebig, Th Lottermoser, D Fröhlich, A V Goltsev, R V Pisarev *Nature (London)* **419** 818 (2002)
18. B K Ponomarev, S A Ivanov, Yu F Popov, V D Negrii, R S Red'kin *Ferroelectrics* **161** 43 (1994)
19. N Hur, S Park, P A Sharma, J S Ahn, S Guha, S-W Cheong *Nature (London)* **429** 392 (2004)
20. Y-H Chu, L W Martin, M B Holcomb, R Ramesh *Mater. Today* **10** (10) 16 (2007)
21. S Czekaj, F Nolting, L J Heyderman, P R Willmott, G van der Laan *Phys. Rev. B* **73** 020401(R) (2006)
22. C Ederer, N A Spaldin *Phys. Rev. B* **71** 224103 (2005)
23. T Zhao, A Scholl, F Zavaliche, K Lee, M Barry, A Doran, M P Cruz, Y H Chu, C Ederer, N A Spaldin, R R Das, D M Kim, S H Baek, C B Eom, R Ramesh *Nat. Mater.* **5** 823 (2006)
24. H Zeng, J Wang, S E Lofland, Z Ma, M L Mohaddes-Ardabili, T Zhao, L Salamanca-Riba, S R Shinde, S B Ogale, F Bai, D Viehland, Y Jia, D G Schlom, M Wuttig, A Roytburd, R Ramesh *Science* **303** 661 (2004)
25. V J Folen, in *Magnetic and Other Properties of Oxides and Relative Compounds* Vol. 3, Pt. 4b (Eds K H Hellwege, A M Hellwege) (Berlin, Heidelberg, New York: Springer,1970) p. 366
26. A J Millis *Nature (London)* **392** 147 (1998)
27. K Dörr *J. Phys. D* **39** R125 (2006)
28. C Thiele, K Dörr, O Bilani, J Rödel, L Schultz *Phys. Rev. B* **75** 054408 (2007)
29. M Fiebig *J. Phys. D* **38** R123 (2006)
30. F Tsui, M C Smoak, T K Nath, C B Eom *Appl. Phys. Lett.* **76** 2421 (2000)
31. W Eerenstein, M Wiora, J L Prieto, J F Scott, N D Mathur *Nat. Mater.* **6** 348 (2007)
32. S Dong, J Zhai, J Li, D Viehland *Appl. Phys. Lett.* **89** 252904 (2006)
33. M N Baibich, J M Broto, A Fert, F Nguyen Van Dan, F Petroff *Phys. Rev. Lett.* **61** 2472 (1988)
34. C L Chien *Annu. Rev. Mat. Sci.* **25** 129 (1995)
35. S Jin, T H Tiefel, M McCormack, R A Fastnacht, R Ramesh, L H Chen *Science* **264** 413 (1994)
36. M Pissas, G Kallias, E Devlin, A Simopoulos, D Niarchos *J. Appl. Phys.* **81** 5770 (1997)

37. J W Lynn, R W Erwin, J A Borchers, Q Huang, A Santoro, J L Peng, Z Y Li *Phys. Rev. Lett.* **76** 4046 (1996)
38. J C Loudon, N D Mathur, P A Midgley *Nature (London)* **420** 797 (2002)
39. P F S Razavi, G Gross, H-U Habermeier, O Lebedev, S Amelinckx, G Van Tendeloo, A Vigliante *Appl. Phys. Lett.* **76** 155 (2000)
40. K H Ahn, T Lookman, A R Bishop *Nature (London)* **428** 401 (2004)
41. C Renner, G Aeppli, B-G Kim, Y-A Soh, S-W Cheong *Nature (London)* **416** 518 (2002)
42. C Israel, M J Calderón, N D Mathur *Mater. Today* **10** (10) 24 (2007)
43. L Zhang, C Israel, A Biswas, R L Greene, A de Lozanne *Science* **298** 805 (2002)
44. W Wu, C Israel, N Hur, S Park, S-W Cheong, A de Lozanne *Nat. Mater.* **5** 881 (2006)
45. P Levy, F Parisi, L Granja, E Indelicrato, G Polla *Phys. Rev. Lett.* **89** 137001 (2002)
46. C Sealy *Mater. Today* **9** 10 (2006)
47. J Z Sun, W J Gallagher, P R Duncombe, L Krusin-Elbaum, R A Altman, A Gupta, Y Lu, G Q Gong, G Xiao *Appl. Phys. Lett.* **69** 3266 (1996)
48. Y Ishii, H Yamada, H Sato, H Akoh *Appl. Phys. Lett.* **89** 042509 (2006)
49. S A Wolf, D D Awshalom, R A Burman, J M Daughton, S von Molnvr, M L Roukes, A Y Chtchelkanov, D M Treger *Science* **294** 1488 (2001)
50. A Ney, C Pumpuch, B Koch, K H Plog *Nature (London)* **425** 485 (2003)
51. J S Moodera, P Le Claire *Nat. Mater.* **2** 707 (2003)
52. J Mathon, A Umerskii *Phys. Rev. B* **63** 220403 (2001)
53. S Yuasa, T Nagahama, A Fukushima, Y Suzuki, K Ando *Nat. Mater.* **3** 868 (2004)
54. M Bowen, V Cros, F Petroff, A Fert, C M Boubeta, J L Costa-Krämer, J V Anguita, A Cebollada, F Briones, J M de Teresa, L Morellón, M R Ibarra, F Güell, F Peiró, A Cornet *Appl. Phys. Lett.* **79** 1655 (2001)
55. LE Hueso, J M Pruneda, V Ferrari, G Burnell, J P Valdés-Herrera, B D Simons, P B Littlewood, E Artacho, A Fert, N D Mathur *Nature (London)* **445** 410 (2007)
56. M Gajek, M Bibes, S Fusil, K Bouzehouane, J Fontcuberta, A Barthélémy, A Fert *Nat. Mater.* **6** 296 (2007)
57. S Chettopadhyay, P Ayyub, V R Patkar, M Multani *Phys. Rev. Condens. Mater.* **52** 13177 (1995)
58. Z L Wang *Mater. Today* **10** (5) 20 (2007)
59. Z W Pan, Z R Dai, Z L Wang *Science* **291** 1947 (2001)
60. J Zhou, N S Zu, Z L Wang *Adv. Mater.* **18** 2432 (2006)
61. P D Yang *Adv. Funct. Mater.* **12** 323 (2002)
62. P X Gao, Y Ding, Z L Wang *Nano Lett.* **3** 1315 (2003)
63. X F Duan, Y Huang, R Agarwal, C M Lieber *Nature (London)* **421** 241 (2003)
64. G F Zheng, F Patolsky, Y Cui, W U Wang, C M Lieber *Nat. Biotechnol.* **23** 1294 (2005)
65. J Song, J Zhou, J L Wang *Nano Lett.* **6** 1656 (2006)
66. W L Huges, Z L Wang *Appl. Phys. Lett.* **82** 2886 (2003)
67. B A Buchine, W L Huges, F L Degertekin, Z L Wang *Nano Lett.* **6** 1155 (2006)
68. R Krimholtz, D A Leedom, G L Matthaei *Electron. Lett.* **6** 398. (1970)
69. S V Vonsovskii *Magnetizm* (Magnetism) (Moscow: Nauka, 1971)
70. A E Clark, B F De Savage, E R Callen *J. Appl. Phys.* **35** 1028 (1964)
71. P de V du Plesis *Phylos. Mag.* **18** 1968 (1968)
72. K B Hathaway, A E Clark *MRS Bull.* **18** 34 (1993)
73. E du T de Lasheiserie *Magnetostriction: Theory and Application of Magnetoalasticity* (Ann Arbor, MI: Chemical Rubber Corp., 1993)
74. N Srisukhumbowornchai, S Guruswamy *J. Appl. Phys.* **90** 5680 (2001)
75. D C Jiles, J B Toelke *Phys. Status Solidi A* **147** 535 (1995)
76. W D Armstrong *J. Appl. Phys.* **81** 3548 (1997)
77. C P Henry, D Bono, J Feuchtwanger, S M Allen, R C O'Handley *J. Appl. Phys.* **91** 7810 (2002)
78. C P Bean, D S Rodbell *Phys. Rev.* **126** 104 (1962)
79. I P Suzdalev *Fiz. Tv. Tela* **12** 988 (1970) [a]
80. I P Suzdalev, V N Buravtsev, V K Imshennik, Yu V Maksimov, V V Matveev, S V Novichikhin, A X Trautwein, H Winkler *Z. Phys. D* **37** 55 (1996)
81. I P Suzdalev, P K Suzdalev *Usp. Khim.* **70** 203 (2001) [*Russ. Chem. Rev.* **70** 177 (2001)]
82. I P Suzdalev, V N Buravtsev, V K Imshennik, S V Novichikhin *Khim. Fiz.* **12** 555 (1993) [b]
83. I P Suzdalev, A S Plachinda, V N Buravtsev, Yu V Maksimov, S I Reiman, V I Khromov, D A Dmitriev *Khim. Fiz.* **17** 104 (1998) [b]
84. I P Suzdalev, Yu V Maksimov, S V Novichikhin, V N Buravtsev, V K Imshennik, V V Matveev *Khim. Fiz.* **19** 105 (2000) [b]
85. I P Suzdalev, Yu V Maksimov, S V Novichikhin, V N Buravtsev, A G Kazakevich, V K Imshennik, V V Matveev *Kolloid. Zh.* **62** 257 (2000) [c]
86. I P Suzdalev, V N Buravtsev, V K Imshennik, Yu V Maksimov *Scr. Mater.* **44** 1937 (2001)
87. I P Suzdalev, V N Buravtsev, Yu V Maksimov, A A Zharov, V K Imshennik, S V Novichikhin, V V Matveev *Izv. Akad. Nauk, Ser. Khim.* 1848 (2003) [d]
88. I P Suzdalev, V N Buravtsev, Yu V Maksimov, A A Zharov, V K Imshennik, S V Novichikhin, V V Matveev *J. Nanopart. Res.* **5** 485 (2003)
89. K Taylor, M Darby *Physics of Rare Earth Solids* (London: Wiley, 1972)
90. A V Shevelkov *Usp. Khim.* **77** 3 (2008) [*Russ. Chem. Rev.* **77** 1 (2008)]
91. R Venkatasubramanian, E Siivola, T Colpitts, B O'Quinn *Nature (London)* **413** 597 (2001)
92. C B Vining *Nature (London)* **413** 577 (2001)
93. G S Nolas J Sharp, H J Goldsmid *Thermoelectrics: Basic Principles and New Materials Developments* (Berlin: Springer, 2001)
94. *Frontiers in Materials Technologies* (Eds M A Meyers, O T Inal) (Amsterdam: Elsevier, 1985)
95. L D Hicks, M S Dresselhaus *Phys. Rev. B* **47** 12727 (1993)
96. L D Hicks, T C Harman, X Sun, M S Dresselhaus *Phys. Rev. B* **53** R10493 (1996)
97. H Ohta, S W Kim, Y Mune, T Mizoguchi, K Nomura, S Ohta, T Nomura, Y Nakanishi, Y Ikuhara, M Hirano, H Hosono, K Koumoto *Nat. Mater.* **6** 129 (2007)
98. J Wood *Mater. Today* **10** 15 (2007)
99. H Ohta *Mater. Today* **10** 44 (2007)
100. G H Jonker *Phyl. Res. Rep.* **23** 131 (1968)
101. J Maier *Nat. Mater.* **4** 805 (2005)
102. A S Aricò, P Bruce, B Scrosati, J-M Tarascon, W van Schalkwijk *Nat. Mater.* **4** 306 (2005)
103. C Jiang, E Hosono, H Zhou *Nano Today* **1** 26 (2006)
104. P Poizot, S Laruelle, S Grugeon, L Dupont, J-M Tarascon *Nature (London)* **407** 496 (2000)
105. J Jamnic *Phys. Chem. Chem. Phys.* **5** 5215 (2003)
106. Y F Zhukovskii, P Balaya, E A Kotomin, J Maier *Phys. Rev. Lett.* **96** 058302 (2006)
107. L Kavan *J. Electrochem. Soc.* **146** 1375 (1999)
108. Y S Hu *Adv. Mater.* **18** 1421 (2006)
109. L Kavan *J. Electrochem. Soc.* **150** A1000 (2003)
110. T Kudo *Solid State Ionics* **152 – 153** 833 (2002)
111. M Hubino, K Abe, M Mochizuki, M Miyayama *J. Power Sources* **126** 139 (2004)
112. H Kawaoka, M Hibino, H Zhou, I Honma *J. Power Sources* **125** 85 (2004)
113. E Hosono, S Fujihara, I Honma, M Ichihara, H Zhou *Electrochem. Commun.* **8** 284 (2006)
114. E Hosono, S Fujihara, I Honma, M Ichihara, H Zhou *J. Electrochem. Soc.* **153** A1273 (2006)
115. E Hosono *International Meeting of Lithium Battaries, Biarritz, France, 2006*
116. I Moriguchi *Adv. Mater.* **18** 69 (2006)

117. S Yang *Solid State Ionics* **90** 281 (1996)
118. M Holzapfel, H Buqa, W Scheifele, P Novak, F-M Petrat *Chem. Commun.* 1556 (2005)
119. D R Smith, W J Padilla, D C Vier, S C Nemat-Nasser, S Schultz *Phys. Rev. Lett.* **84** 4184 (2000)
120. V G Veselago *Usp. Fiz. Nauk* **92** 517 (1967) [*Physics-Uspekhi* **10** 509 (1968)]
121. M C K Wiltshire *Science* **291** 849 (2001)
122. T J Yen *Science* **303** 1494 (2004)
123. C Enkrich, M Wegener, S Linden, S Burger, L Zschiedrich, F Schmidt, J F Zon, Th Koschny, C M Soukoulis *Phys. Rev. Lett.* **95** 203901 (2005)
124. E Hecht *Optics* (4th Ed.) (Massachusetts: Addison-Wesley, 2001)
125. W J Padilla, D N Basov, D R Smith *Mater. Today* **9** 28 (2006)
126. J B Pendry *IEEE Trans. Microw. Theory Tech.* **47** 2075 (1999)
127. S Linden, C Enkrich, H Wegener, T Zhou, T Koschy, C M Soukolis *Science* **306** 1351 (2004)
128. T M Grzegorczyk *IEEE Trans. Microw. Theory Tech.* **53** 1443 (2005)
129. D R Smith, D C Vier, W Padilla, S C Nemat-Nasser, S Schultz *Appl. Phys. Lett.* **75** 1425 (1999)
130. R A Shelby, D R Smith, S Schultz *Science* **292** 77 (2001)
131. S Zhang, W Fan, N C Panoiu, K S Panoiu, K J Malloy, R M Osgood, S R J Brueck *Phys. Rev. Lett.* **95** 137404 (2005)
132. A Pimenov, A Loidl, K Przyslupski, B Dabrovskii *Phys. Rev. Lett.* **95** 247009 (2005)
133. W J Padilla, A J Taylor, C Highstrete, M Lee, R D Averitt *Phys. Rev. Lett.* **96** 107401 (2006)
134. C L Holloway, E F Kuester, J Baker-Jarvis, P Kobos *IEEE, Trans. Antennas Propag.* **51** 2596 (2003)

[a] — *Phys. Solid State (Engl. Transl.)*
[b] — *Russ. J. Phys. Chem. B (Engl. Transl.)*
[c] — *Colloid J. (Engl. Transl.)*
[d] — *Russ. Chem. Bull., Int. Ed. (Engl. Transl.)*